A STUDY OF THE OCEAN CIRCULATION OFF THE COAST OF CHILE
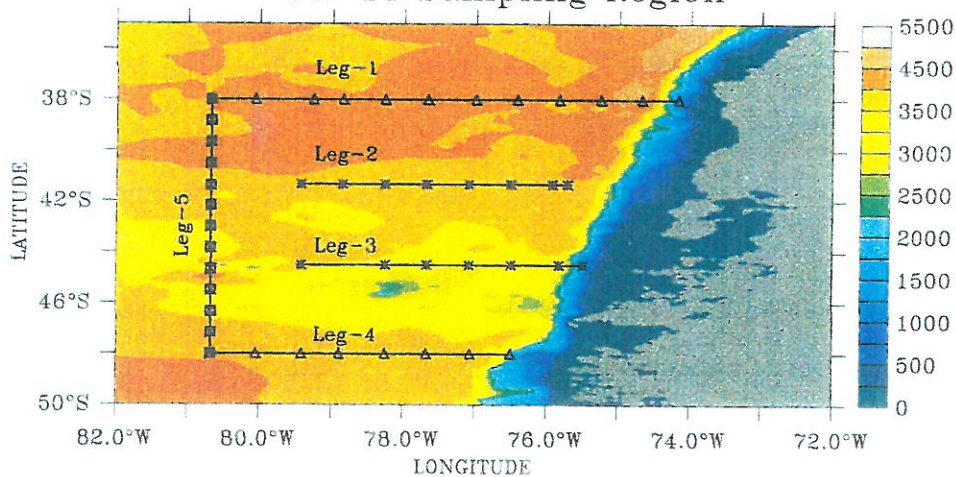
BY

RODRIGO H. NUÑEZ

DEPARTMENT OF OCEANOGRAPHY
SERVICIO HIDROGRAFICO Y OCEANOGRAFICO
ARMADA DE CHILE
ERRAZURIZ 232 PLAYA ANCHA, VALPARAISO - CHILE

World Ocean Circulation Experiment PR-14 Sampling Region

DECEMBER 1996

TECHNICAL REPORT 96-4

TABLE OF CONTENTS

FOREWORD

This is a unique oceanographic study. It combines the results of several cruises by the small country of Chile and the computer power of the U.S. Navy's excellent global ocean model. This is the Ph.D. Thesis of Lt. Commander Rodrigo Nuñez, Chilean Navy. Mr. Nuñez analyzed and interpreted the Chilean hydrographic data at 44°S off Chile. The NRL Ocean Model data was provided to compare with the ocean data.

Both data sources compliment each other. The hydrographic data accurately depicts the main distribution and the potential vorticity distribution. The patterns found are new and do not agree with previous concepts.

The numerical model demonstrates how the bottom topography steers the flow and how the seasonal shifts of the wind field modifies the current distribution in the study area.

Even today with massive experiments such as WOCE and terribly expensive satellites like Topex ,one rarely gets the picture of the ocean dynamics as found in this investigation.

James J. O'Brien
Professor
Meteorology and Oceanography
Director, COAPS

ABSTRACT

This study presents the results of an ambitious oceanographic program carried out as the Chilean contribution to the World Ocean Circulation Experiment (WOCE).

Data collected during the WOCE PR-14 cruises has been used to describe and study, for the first time, the structure and variability of the eastern boundary current system of the South Pacific Ocean. In the region where the Antarctic Circumpolar Current (West Wind Drift) bifurcates, forming the Humboldt Current and the Cape Horn Current, transport calculations have been carried out to estimate the transport into each branch and the temporal variability of the transport. The results obtained from the hydrographic data show that the eastward transport into the WOCE PR-14 Sampling Region is almost constant.

The WOCE PR-14 cruises contain information of a short period of time every year, leaving unresolved an important part of the seasonal variability. Therefore, a numerical model, developed at the Naval Research Laboratory, has been used to complement the results derived from the analysis of the hydrographic data. The NRL finite-depth model yields a realistic representation of the temporal and spatial variability of the eastern boundary current system of the South East Pacific Ocean. Bottom topography is shown to produce a considerable steering effect on the currents

of the region, exerting a controlling influence on the main features of the South Pacific Eastern Boundary System, such as the turning point of the Antarctic Circumpolar Current into the Humboldt Current.

The results of this study show that the goals of the WOCE PR-14 cruise have been achieved. A useful description of the ocean behavior of the transition zone (circulation and transport) has been made using the data collected during 1993, 1994 and 1995. The location of the bifurcation of the Antarctic Circumpolar Current has been found and some of the physical processes involved have been described and studied.

1. INTRODUCTION

Chile possesses 4,200 km of the southwestern coastline of South America. It has an almost meridional coastline with a steady equatorward wind stress. The Southeast Pacific boundary current system (an upwelling system) is recognized as one of the most biologically productive areas of the global ocean. The region of high productivity extends from 5°S off Peru to 40°S off southern Chile. The volume of fish caught in the Pacific Ocean is more than two times the combined volume of fish caught in the Indian and Atlantic Oceans (Parfit, 1995). Of the 52 million metric tons captured in the Pacific Ocean in 1992, 14 % was captured off the Chilean coast and the combined captures of Chile and Peru accounted for 30% of the total catch - enough fish to supply United States, Russia and India, or China for one calendar year. Chile exports more fish meal than any other country in the world and has long relied on the national fishing industry as a significant factor in its economy. Yet, in spite of its obvious importance, the water masses and currents south of 15°S are poorly known (Fonseca, 1989; Neshyba and Mendez, 1976).

For the past 35 years, several attempts to study the circulation off Chile have been carried out by Chilean and foreign scientists. Most of the studies have been related to the northern upwelling region of Peru-Chile, north of 20°S (Huyer et al, 1991; Brink et al, 1983; Wyrtki, 1963), the extension of the Peru-Chile

1

Undercurrent (sometimes referred as the Gunther Undercurrent, Silva and Neshyba, 1979) and the West Wind Drift (Neshyba and Fonseca, 1980).

In 1967 and 1968 two major transpacific hydrographic sections at latitudes 43°S and 28°S were made as part of the SCORPIO expedition (Eltanin cruises 28 and 29, respectively). These two transects were laid out with observation of the deep circulation of the Pacific Ocean as their principal objective. The first leg (Cruise 28) was the first ever made with closely spaced stations (100 miles in open sea, 50 miles over complex bottom topography) all the way across the Pacific. As a result of the ELTANIN cruises, the first dynamic computations of geostrophic velocity were carried out using the deep SCORPIO data, with an assumed level of no horizontal motion at 2 km (Warren, 1973). The calculated fields of geostrophic velocities have been used since then as the only "updated" reference to plan any subsequent studies of the Southeast Pacific.

Until 1985, when the World Ocean Circulation Experiment (WOCE) program was designed and implemented, no systematic oceanographic cruises were ever done with the specific purpose of studying the main features of the ocean circulation off Chile.

The World Ocean Circulation Experiment is a major component of the World Climate Research Program (WCRP) sponsored jointly by intergovernmental and non-intergovernmental organizations. WOCE is a multinational eight-year effort (1990-1997) by scientists from more than 30 nations to study the large-scale circulation of the ocean. WOCE employs several satellites, dozens of ships, and

2

thousands of instruments to obtain a basic description of the physical properties and circulation of the global ocean during a limited period.

The WOCE Science Steering Group has set two goals for the experiment (WCRP Report No. 6, 1986). These goals are:

Goal 1: To develop models useful for predicting climate change and to collect the data necessary to test them.

Goal 2: To determine the representativeness of the specific WOCE data sets for long-term behavior of the ocean, and to find methods for determining long-term changes in the ocean circulation.

In order to achieve Goal number 1 and 2 several oceanographic cruises were planned by the International WOCE office and the U.S. WOCE office.

Cruises through the nearly unexplored system of eastern surface boundary currents and eastern boundary undercurrents were planned as part of the study of the circulation in the South Pacific Ocean. Unlike northern oceans, where the west wind drift splits into subtropical and subpolar recirculations, the poleward branch along South America may either enter the Drake Passage and flow to the Atlantic Ocean or recirculate in the subtropical gyre. Thus the bifurcation is important to interocean exchanges of mass and heat (US WOCE Planning Report No. 3, 1986).

Two related objectives addressing the mid-latitude boundary currents of the South Pacific Ocean that are part of WOCE were defined:

a) To describe the structure and variability of the eastern boundary current system (The Humboldt Current (HC) or Peru-Chile Current,

3

The Cape Horn Current (CHC) and the Gunther Undercurrent (GUC) or Peru-Chile Undercurrent).

b) In the region where the west wind drift (WWD) bifurcates, forming the Humboldt and Cape Horn eastern boundary currents, estimate the transport of each branch and the time variations in transport.

WOCE cruise PR-14 (a repeated hydrographic cruise) was planned and designed to study an enclosed area of the Southeast Pacific Ocean where, supposedly, the WWD divides upon impinging the coast of South America, and to gain a more useful description of ocean behavior in this important transition zone.

The first two WOCE PR-14 cruises (1991-1992) were made on board of the AGS Yelcho, a former US Navy towing ship, barely conditioned to be a research vessel with one propeller and no horizontal stabilizers, using Niskin bottles. In 1992, the US Navy, through the Office of Naval Research (ONR), transferred the AGOR 10 Thomas Washington from SCRIPPS to the Chilean Navy. Since 1993 the WOCE PR-14 cruises have been made on this ship (now AGOR Vidal Gormaz) using Nansen bottles and CTD's. The cruises are scheduled once a year and will end in October of 1997.

The temporal distribution of the WOCE PR-14 cruises will allow us to describe the structure and variability of the Humboldt Current, the Cape Horn Current and the Gunther Undercurrent. At the same time, transport calculations will be done to look at the variations in transport of the Humboldt Current and Cape Horn Current.

4

A high resolution numerical ocean model is used to analyze the seasonal variations in the circulation and to complement the results derived from the analysis of the hydrographic data, due to the fact that the WOCE PR-14 cruises were only carried out once a year, at the end of the southern spring (1993-1994) and southern winter (1995),

The model used in this research is one of the Naval Research Laboratory models, best known as the Navy layered model or as the NRL model. The NRL model is a hydrodynamic (isopycnal) nonlinear, primitive equation, layered ocean circulation model (Wallcraft, 1991). The NRL model has been successfully used to study the circulation in regions such as the Indian Ocean, the North Atlantic Ocean, the North Pacific Ocean and the Sea of Japan. The results of the NRL model used in this research correspond to a subregion of the global ocean model (Fig. 1a) that includes the area sampled during the WOCE PR-14 cruises (Fig. 1b). The model simulation covers the period from 1981 through 1995.

The main objective of this research is to obtain a better understanding of the temporal variability of the West Wind Drift and of the ocean circulation off Chile. The organization of this study is as follows: Chapter 2 describes the results obtained from the hydrographic data collected during the WOCE PR-14 cruises. Temperature, salinity and density profiles are analyzed and a physical description of the results is given. The calculated fields of geostrophic velocities, potential vorticity and transport are presented and discussed. Chapter 3 includes a description of the numerical model and an analysis of the modeling experiment, along with a comparison

of model results with the WOCE PR-14 observations. Chapter 4 contains the conclusions and summary of the study. The results of the analyses of the hydrographic data and the numerical simulation are combined in this chapter to present the main features of the ocean circulation and transport off Chile.

2. WORLD OCEAN CIRCULATION EXPERIMENT PR-14

2.1 Hydrographic Data

The data set used in this study has been collected during the WOCE PR-14 cruises carried out on the R/V AGOR "Vidal Gormaz" of the Chilean Navy. Only the data of the last three cruises (1993, 1994 and 1995) are used in this analysis. The data collected in 1991 and 1992 were not used due to severe quality control problems. The first two cruises of this series were made on an old towing ship using Niskin bottles with no ability to keep the ship from drifting away from the station during mild weather conditions. The 1993 cruise has three legs: leg 1 along latitude 38°S, leg 2 along latitude 48°S and leg 3 along longitude 82° 15'W, linking legs 1 and 2 and closing the rectangle. The cruise was carried out between October 7 and October 16. The averaged maximum depth in 1993 was around 1400 meters. The distance between each pair of stations is about 30 minutes of latitude (30 nautical miles). In 1994 and 1995 two latitudinal legs were added to improve resolution in the interior of the rectangle and to facilitate transport calculations along the north-south leg. These two new legs run along latitude 41° 30'S and 44° 20'S. The maximum depth of the stations in 1994 and 1995 was around 3500 meters, with the exception of the stations on the continental platform that were limited to a safe depth over the sea floor. The north-south leg (now leg-5) was moved from 82° 15'W to 80° 40'W to

keep the number of stations below 50 and not to extend the duration of the cruises for more than 20 working days at sea. The 1994 cruise was carried out between October 6 and October 22. The 1995 cruise was carried out between May 28 and June 14.

Figure 2 shows the cruise tracks for 1993 and 1994-1995. The geographic location of the hydrographic station are indicated with symbols on each one of the legs. It is clear that the spatial coverage was greatly improved with the addition of legs 2 and 3 in 1994 and 1995. The color bar on the right hand side indicates ocean depth in meters.

2.2 Data Set Description

CTD (Conductivity-Temperature vs. Depth) data were collected with a Sea-Bird SBE-09 CTD (1995) and with a Sea-Bird SEACAT SBE-19/02 CTD (1993 and 1994) which have an internal Digital Quartz pressure sensor and external temperature and conductivity sensors. These CTD's have a temperature-conductivity duct, which is used to circulate sea water through both the temperature and conductivity sensors. The CTD was mounted on a 24-bottle (2.5 liters) rosette sampler, and the package was deployed on a hydrographic (3-conductor) cable, which allowed for real-time data acquisition and data display. Water samples were taken at standard depths on the upcasts for chemical analyses, and for calibration of the conductivity sensor. Digital data were recorded on a PC-compatible computer.

The data were subjected to quality control procedures and preliminary processing. First they were screened for spikes or missing data. After screening, the

8

data were filtered using a low pass filter to produce zero phase (no time shift). This process forced conductivity to have the same time response as temperature. The next step was to align temperature and conductivity measurements in time relative to pressure. This ensures that calculations of salinity and other parameters are made using measurements from the same parcel of water. The data were then averaged to half-second values, and the pressure, temperature and conductivity calibration corrections were applied (SHOA, Data Report, 1997).

The measured parameters pressure, temperature and conductivity were then used to compute the following parameters: salinity, density, potential temperature, specific volume anomaly, depth, geopotential anomaly and dynamic height. The formulas for the computation of salinity, density, potential temperature and specific volume anomaly were obtained from Fofonoff and Millard (1983).

2.2.1 Salinity

The salinity along latitude 38° 00' S in 1994 (leg-1 on figure 2b) in 1994 shows a well defined and narrow zone of upwelling bordering the coast that extends out to longitude 74° 30' W. The same phenomenon is seen in 1993 and 1995. The minimum values in the vertical distribution are found at the surface (upper 30 meters) and corresponds to waters coming from the Chilean Inland Seas through the Chacao Canal (latitude 41° 50' S) and Gulf of Corcovado (latitude 43° 30' S). These low salinity waters are produced by high levels of precipitation over the entire region that averaged to 2.5 m/yr (Strub et al., 1996) and generate an

9

important runoff flow into the Inland Seas. In 1994 the salinity low was around 33.5‰ (ppt), but it could be as low as 31-32‰ depending on the season and meteorological conditions.

Figure 3 shows a core of denser water (34.7-34.8‰) close to the coast at a depth of 150 to 350 meters. This water is not being upwelled from depths of 1300 meters because the permanent thermocline is centered around 1000 meters, but probably is advected from the coast. A core of salinity 34.5-34.6 ‰ is found centered at longitude 79° 20' W between depths of 280 and 330 meters.

The salinity along latitude 41° 30' S (leg-2 Figure 2b) shows almost the same characteristics as leg-1 (Figure 4). The upwelling is less pronounced and still confined to the first 100 kilometers off the coast; the lower salinity layer at the surface extends farther off the coast and deeper (50 meters); the core of denser water has a density of 34.5-34.6 ‰, an average depth of 300 metes, and it could have been upwelled from a depth of 800 meters. A core of this denser water is also found centered at longitude 78° 15' W between depths of 240 and 370 meters.

The salinity along latitude 44° 20' S (leg-3 Figure 2a) shows the layer of low salinity closer to the coast and shallower (upper 25 meters) than in leg-2 (Figure 5). The coastal region is neither an upwelling nor downwelling region. The core of denser water is now centered at 250 meters and longitude 76° 20' W.

The salinity along latitude 48° 00' S (leg-4 Figure 2b) shows a well defined downwelling region in a narrow area of 100 kilometers off the coast (Figure

10

6). The surface layer of lower salinity covers the first 150 kilometers off the coast with minimum values of 31.5‰. The fresh water at this latitude comes from large glaciers located at latitude 47° S and latitude 49° S. These glaciers and the precipitation runoff come out through the Gulf "de Penas" at latitude 47° 30' S into the Pacific Ocean. The core of denser water found in the previous profiles is not present at this latitude, and neither is seen in the same profiles of the 1993 and 1995 cruises.

The salinity along the meridional transect (leg-5 Figure 2b) shows a surface layer of 33.8‰ that goes from 41° 15' S to 47° 30' S with an average depth of 60 meters (Figure 7). This layer is found in 1993 along leg-3 (Figure 2a) at a shallower depth (around 40 meters) and with a narrower meridional extension. In 1995 the surface layer is of the same characteristics as in 1994, but it starts at latitude 41° 20' S and extends outside of the surveyed region, south of leg-4. A core of salinity 34.5-34.6‰ is found at latitude 38° 40' S between depths of 280 and 380 meters.

2.2.2 Temperature

The temperature profile along leg-1 in 1994 shows a subsurface layer of 12.5-13.0 ° C that is shallower close to the coast (15 meters) in the upwelling zone deepens towards the west (Figure 8). This subsurface layer outcrops at latitude 79° 30' S and between latitudes 75° 30' S and 76° 30' S at the same locations where waters of salinity 33.8-33.9 ‰ reach the surface. At the core of the denser water, found at a depth of 150-350 meters in figure 3, the isotherms have a negative slope that compensate the positive slope of the isohalines, resulting in a stable stratification. The

11

maximum temperature at the surface is 13.57° C. In 1995, the maximum temperature at the surface is 16.0° C (Figure 9) and the average temperature of the upper 80 meters is 2° C warmer than the values recorded in 1993 and 1994. Both figures show coastal upwelling and a westward deepening of the warmer surface layer. The warmer surface waters of May-June 1995 (austral fall) are a result of the surface heating received during the summer months (Jan-Feb-Mar) and autumn winds (stronger than in summer), that combined with the coastal upwelling of colder water tilted the thermocline and started to cool down the adjacent water off shore.

As we progress southward the temperature profiles along legs 2, 3 and 4 show characteristics that are similar to the ones found in the salinity profiles in regard to upwelling and downwelling. The temperature in the upper 300 meters decreases southward by 2.5° C in Spring (1993, 1994) and by 5.5° C in Fall (1995). In 1995, the warmer surface layer is present in all the stations along the latitudinal legs, but in 1993 and 1994 it moves closer to the coast toward the south leaving the western part of leg-4 colder than the coastal waters. The offshore negative temperature gradient of the surface layer on legs 3 and 4 (1993, 1994) is produced by outflow of warmer and fresher surface water from the Chilean Inland Seas through the Gulf of Corcovado and Gulf "de Penas".

The vertical distribution of temperature along the meridional transects show higher surface temperatures equatorward (positive northward) gradient (Figure 10, 1994; Figure 11, 1995). This result is consistent with the longer heating time and more direct incidence of solar radiation that lower latitudes have in comparison with

higher latitudes; i.e. shorter summers in higher latitudes. The latitudinal extension and the temperature of the warmer waters are related to the time of the year when the measurements are made. The 1993 and 1994 cruises were completed during the first month of spring after a long period of surface cooling and strong winds. In the other hand, the 1995 cruise was completed in June, before the start of winter season when the meteorological conditions favored a well defined mixed layer.

In figure 10 we see a deep mixed layer at around a depth of a 100 meters along the northern part of the transect and a much shallower thermocline along the southern part. In contrast, figure 11 shows a deeper mixed layer that decreases in depth from 120 meters at the northern most station to 90 meters at the southern most station. Figures 10 and 11 show that the vertical gradient of temperature decreases southward along longitude 80° 40' W, but the vertical gradient is much larger in 1995 than in 1994. This difference is, as explained in the previous paragraph, a direct result of the seasonal and latitudinal changes in heating and mixing conditions associated with the local winds.

2.2.3 Density (Sigma-Theta)

All the density plots generated with the data collected during the PR-14 cruises have a remarkable similarity: they show a stable stratified ocean. The vertical distribution of density shows the dynamic signal of upwelling and downwelling produced by local winds and present in both the salinity and temperature records. The flux of fresher water coming from the Chilean Inland Seas produced by precipitation

runoff and ice melting creates a surface layer of lighter water that moves along shore and/or off shore depending on the wind conditions.

A cross shelf section of density versus depth for leg-1 in 1994 is shown in figure 12. The vertical distribution of density indicates a well stratified ocean with a narrow region of upwelling along the coast and a tongue of fresher water in the upper 20 meters that extends off the coast to longitude 75° 30' W. The low density water found at the western most part of the transect is produced by the combination of relatively low salinity (Figure 3) and warmer water (Figure 8). Other features, such as the bump found between 100 and 300 meters and longitudes 74° 30' W and 75° 30' W, can also be explained by the same elements.

Figure 13 shows the vertical distribution of density along leg-5 in 1994. The effect of the larger vertical temperature gradient in the upper 300 meters, especially in the southern most part of the transect, produces a density distribution with lower density waters near the northern boundary than at the southern boundary. The upper 300 meters show a positive latitudinal gradient toward the south and a vertical gradient that decreases in the same direction. From figures 7 and 10 we can conclude that for depths $\leq$ 300 meters the density structure is dominated by temperature (i.e. the isopycnals closely follow the shape of the isotherms) and for $300 \leq$ depths ≤ 1400 meters the density structure is dominated by salinity (i.e. the isopycnals closely follow the shape of the isohalines).

2.2.4 Geostrophic Velocity

The relative velocities are calculated using the geostrophic method described in Pond and Pickard (1986). The subroutines used to calculate the specific volume anomalies and the conversion of depth to pressure, based on the hydrographic data collected during the WOCE PR-14 cruises, were obtained from Fofonoff and Millard (1983). All geostrophic velocities calculated between any two adjacent stations A and B are perpendicular to the line AB. The resulting velocity follows conventional oceanography signs: positive implies northward or eastward velocity; negative implies southward or westward velocity. The geostrophic velocity is found using:

$$(V_1 - V_2) = \frac{1}{L2\Omega\sin\phi}\left[\int_{P_1}^{P_2}\delta_B dp - \int_{P_1}^{P_2}\delta_A dp\right] = \frac{1}{L2\Omega\sin\phi}\left[\Delta\Phi_B - \Delta\Phi_A\right] \qquad (2.1)$$

all symbols used in equation (2.1) are as defined in section 8.42 of Pond and Pickard (1986).

The reference level chosen for this calculation is 1000 meters (LNM = level of no motion). This level was chosen for the following reasons: (1) previous studies of the area had used 1 km as the LNM (Reid, 1965); (2) some stations were limited by topographic features to depths close to 1 km; (3) vertical distribution of isotherms and isohalines show that the slopes of these properties almost disappear near 1 km. This choice of level is not thought to be exact or correct everywhere, but it seems roughly appropriate for these sections.

The upper 300 meters of the calculated geostrophic velocity fields for the 1994 WOCE PR-14 cruise show two northward coastal currents crossing leg-2

at longitudes 75° 40' W and 76° 50' W (Figure 15), and one northward coastal current crossing leg-1 at longitude 75° 30' W (Figure 14). In both cases the strongest current is the one closer to the coast (6-12 cm/s). Along leg-3 (Figure 16) and leg-4 (Figure 17) this situation is reversed, with a poleward current (southward) that extends from the coasts out to longitude 77° 45' W. Along 78° 00' W there exists a narrow northward current, almost negligible across leg-3, but of an intensity of 7-9 cm/s across leg-4. Across leg-5 three well defined eastward currents and two westward currents are found (Figure 18). The strongest of the eastward currents is centered around latitude 44° 00' S and reaches a maximum intensity of 9-10 cm/s. The two westward currents have a width of about 100 km and are located between latitudes 41° 40' S and 46° 00' S.

The currents between 300 and 1000 meters are of the order ±1-2 cm/s. The only two exceptions to this generalization occur along leg-4 (Figure 17) where we find the coastal poleward current penetrating all the way down to 600 meters with intensities of 3-4 cm/s, and a deep northward current centered at 580 meters and longitude 76° 45' W with intensities of 4-5 cm/s.

There is a clear reversal in the direction of the coastal currents between leg-2 (41° 30' S) and leg-3 (44° 20' S). The change in the direction of the coastal currents associated with the first baroclinic mode was already insinuated during the analyses of the salinity, temperature and density profiles. Areas of upwelling (downwelling) and low surface salinity waters were found along all north-south legs near the coast. As a result of these two factors the slope of the isopycnals along the coast changed from positive (leg-1 and leg-2, upwelling - equatorward flow) to

16

negative (leg-3 and leg-4, downwelling - poleward flow) and the vertical density gradient was much larger in this narrow zone than offshore.

Figure 19 shows the averaged surface wind stress for the South East Pacific Ocean during the same period of the WOCE cruise PR-14 in 1994 (10/06/96 to 10/22/94). The 6-hour interval data used to calculate the wind stress was obtained from the European Center for Medium Range Weather Forecast (ECMWF). All values at each geographic location were averaged for the 17 day period of the cruise to produce figure 19. The winds at longitude 75° 22.5' W (near the coast) and between latitudes 38° 00' S and 48° 00' S change direction from ENE to ESE (direction in which the wind blows) as we move poleward. The transition latitude, where the winds are parallel to the E-W axis, is located around latitude 42° 00' S (between leg-2 and leg-3). The direction of the winds along the coast is consistent with the upwelling and downwelling conditions found in the hydrographic data. The "bifurcation" of the winds at latitude 42° 00' S is produced by the interaction of the South Pacific High (denoted by "H" in figure 19) centered at 31° 00' S and 98° 00' W, the Amundsen Sea Low centered at 75° 00' S and 110° 00' W (west of the Antarctic peninsula - not shown in figure 19; Chen et al, 1996) and the Andes mountains.

2.2.5 Potential Vorticity

Potential vorticity maps are plotted using a finite-difference form of the large-scale potential vorticity as described in McDowell et al., (1982). A review of this theory and its application can be found in Pedlosky (1996).

In general, for an isopycnal layer of thickness Δz, the potential vorticity "q" on the planetary scale is simply:

$$q = f \frac{\Delta \sigma_\theta}{\Delta p} g \qquad (2.2)$$

where f is the Coriolis frequency, g is the acceleration due to gravity, $\Delta \sigma_\theta$ is the chosen vertical increment, in parts per thousand, of the potential density σ_θ (referenced here to the surface) and Δp the thickness in decibars of the σ_θ interval. The interval $\Delta \sigma_\theta$ is chosen to be large enough to suppress noise in the data (i.e. below the seasonal thermocline) but still above the permanent thermocline.

The finite-difference form of equation (2.2) can be obtained starting from the continuous representation of the potential vorticity equation (2.3) and the hydrostatic equation (2.4).

$$q = \frac{f}{\rho_0} \frac{\partial \rho}{\partial z} \qquad (2.3)$$

$$\frac{\partial p}{\partial z} = -\rho_0 g \quad \text{or} \quad \frac{1}{\partial z} = -\frac{\rho_0 g}{\partial p} \qquad (2.4)$$

where z is the vertical coordinate and ρ_0 is a reference density. Substitution of (2.4) into (2.3) gives equation (2.5), where density is the vertical coordinate and the derivatives have been replaced by finite differences.

$$q = f \frac{\Delta \rho}{\Delta p} g \qquad (2.5)$$

Replacing $\Delta \rho$ by $\Delta \sigma_\theta$ makes it possible to calculate potential vorticity directly from the density field without any reference to the velocity field. Maps of

18

potential vorticity fields are a invaluable tool in the discussion of the general circulation, as they can be interpreted as flow paths (Keffer, 1985).

Three maps of potential vorticity are presented in this section. These maps correspond to the WOCE PR-14 1994 cruise. The values of potential vorticity calculated at each station, between two predefined isopycnals, were linearly interpolated to create a two dimensional field that covers the same region as the PR-14 sampling area. The values of the isopycnal surfaces chosen were 26.2, 26.7 and 27.2 kg/m^3. The 26.2 kg/m^3 isopycnal has a maximum depth of 200 meters and outcrops near the intersection of leg-4 and leg-5, as it can be seen in figure 13. The intermediate isopycnal of 26.7 kg/m^3 resembles the shape of the 26.2 kg/m^3 isopycnal, with maximum depths along leg-1 and minimum depths near the intersection of leg-4 and leg-5. The depth range for this isopycnal is between 120 and 300 meters. The deeper 27.2 kg/m^3 isopycnal has a depth range between 740 and 900 meters. The minimum depth is founded at the eastern most station on leg-1 (Figure 12) and the maximum values are near the intersection of leg-2 and leg-5. Column thickness between $\sigma_\theta = 26.2$ and $\sigma_\theta = 26.7$ ranges from 80 to 190 meters; column thickness between $\sigma_\theta = 26.7$ and $\sigma_\theta = 27.2$ ranges from 460 to 720 meters; and column thickness between $\sigma_\theta = 26.2$ and $\sigma_\theta = 27.2$ ranges from 620 to 860 meters.

The interpolated potential vorticity fields have a few arbitrary contour lines superimposed on the color-filled contour plot to help the identification of the proposed flow paths. The direction of the flows (currents) are not discussed in the following analysis, only the path that the flow follows inside the PR-14 region. A consolidated analysis is presented in the discussion section at the end of the chapter,

where all the variables analyzed are combined to obtain a physical description of the circulation in this important area of the Pacific ocean.

Figure 20 presents the interpolated potential vorticity field calculated between the upper (shallower) 26.2 isopycnal surface and the lower (deeper) 27.2 isopycnal surface. Using the contour lines superimposed on the field it is possible to identify one flow along the coast in the north-south direction and another flow that comes in (or out) between latitudes 41° and 43° S along longitude 80° 40' W and bifurcates (or converges) into (or from) two north-south branches. The potential vorticity field observed in this figure corresponds to the upper 900 meters of the water column and includes the main features in this layer. To obtain a better identification of the flows further refinements in the interval $\Delta\sigma_\theta$ are performed.

Figures 21 and 22 show the potential vorticity fields of the upper 300 meters and lower 300-900 meters, respectively. The interval $\Delta\sigma_\theta$ between 26.2 and 26.7 kg/m^3 (Figure 21) shows an east-west flow coming in (or out) around latitude 43° S along leg-5 and bifurcating (or converging) into two north-south branches; a second flow that meanders along the coast can be seen entering (or exiting) leg-4 at longitude 76° 30' W, moving close to the coast about latitude 42° S and exiting (or entering) leg-1 at longitude 77° W. The deeper interval $\Delta\sigma_\theta$ between 26.7 and 27.2 kg/m^3 (Figure 22) shows a north-south flow of a width of about 100 km that moves along the coast and a second, less defined north-south flow, that enters (or exits) leg-4 at longitude 79° 30' W, moves eastward as it progresses northward and exists (or enters) leg-1 at longitude 77°-78° W.

The separation into two sub-layers shows that figure 20 lacks the necessary vertical resolution to describe some of the circulation features of the region, but retains two main strong characteristics: a north-south coastal flow and an east-west bifurcation (or convergence). The sub-layers appear to be refined enough to cover a single flow regime and to provide a useful description of the surface currents and undercurrents in the region.

2.2.6 Transport

Transport calculations were done using the geostrophic velocities calculated with a reference level of 1000 meters. A vertical integration of the velocities was performed, from the assumed level of no motion to the surface, to obtain the flux per unit depth at a half way point between each pair of hydrographic stations. The next step was to calculate the distance between each pair of collocated half way points and then, multiplied this distance by the averaged of the fluxes per unit depth at the same pair of points to obtain the vertically integrated transport.

In order to compare the 1993 cruise with the 1994 and 1995 cruises, the two western most stations of leg-1 and leg-2 (see figure 2a) were left out of the calculations of latitudinal transport and leg-3 was assumed to be located at the same longitude of leg-5 in 1994 and 1995 (see figure 2b).

The last step in the calculation was to adjust the net flow inside the rectangles defined by leg-1, leg-4 and leg-5 equal to zero. The adjustment was performed using a least square fitting formulation with side boundary constrains. The

21

side boundary constrains were such that the net flow inside each one of the smaller rectangles defined by leg-1, leg2, leg-5 (box-1); leg-2, leg-3, leg-5 (box-2); and leg-3, leg-4, leg-5 (box-3) was equal to zero, too. The transport along the southern boundary of the rectangles, i.e. the line that joins the southern most stations of each latitudinal leg, was set to zero. Figure 23 shows a schematic diagram of the rectangles used in the calculations.

The following equation was used for the least square fitting of the total net transport and the individual net transports in each box:

$$F\left(\lambda_i, \Delta T_j\right) = \sum_{i=1}^{3}\left[\sum_{j=1}^{M}\left(\frac{1}{2\sigma_j^2}\right)\left(\Delta T_j - \Delta T_j'\right)^2 + \lambda_i B_i\right] \qquad (2.6a)$$

$$B_i = \sum_{j=1}^{N_i}\left(\frac{\Delta T_j}{\Delta j}\right) \qquad i = 1, 2, 3 \qquad (2.6b)$$

where:

i = box index number (1, 2 or 3).

j = station index number.

λ_i = lagrangian multiplier associated to box i (unknown).

ΔT_j = adjusted vertically integrated transport at station j (unknown).

$\Delta T_j'$ = observed vertically integrated transport at station j.

σ_j^2 = variance of $\Delta T_j'$ at station j.

B_i = total observed net flux per unit length in box i.

N_i = number of stations in box i.

M   = sum over the perimeter of box 1, box 2 and box 3.

$F\left(\lambda_i, \Delta T_j\right)$ = cost function to be minimized.

The results of the least square fit are presented in table 1. The definition of the boxes and the sides is in figure 23.

Table 1: Vertically Integrated-Adjusted Transport obtained from the least square fit analysis. Transport is given in Sverdrups [Sv]. 1 Sv = 10^6 m³/s. Arrows after transport values indicate direction of the flow. ↑ = Northward, ↓ = Southward, → = Eastward and ← = Westward. Shaded cells are used to indicate a reversal in the flow direction or to highlight each transport box.

			WOCE PR-14 1993 [Sverdrups]	WOCE PR-14 1994 [Sverdrups]	WOCE PR-14 1995 [Sverdrups]
Box 1		Side I	2.90 ↑	2.95 ↑	2.58 ↑
Box 1		Side V	0.79 →	0.54 →	0.30 ←
Box 1	Box 2	Side II	N/A	2.41 ↑	2.88 ↑
Box 2		Side VI	3.04 →	3.44 →	3.29 →
Box 2	Box 3	Side III	N/A	1.03 ↓	0.41 ↓
Box 3		Side VII	0.25 ←	0.29 ←	0.35 →
Box 3		Side IV	0.68 ↓	0.74 ↓	0.76 ↓
Net Transport across long. 080° 40' W		Side V+VI+VII	3.58 →	3.65 →	3.34 →

Some of the most important characteristics of the transport are:

a) The net transport along longitude 80° 40' W remains almost constant from year to year. The change in transport between spring (1993 and 1994 cruises) and fall (1995 cruise) is less than 10% of the 1994 transport.

b) Surface transport, first 150 meters of the water column above the seasonal thermocline, accounts for an average 17% of the total net transport across the north-south leg of the cruises.

c) In the three cruises the largest part of the eastward transport comes into the region between latitudes 41° 30' S and 44° 20' S (leg-2 and leg-3, respectively).

d) The north-south transports have the same directions across each leg during each of the three year periods of the observation.

e) The results of the transport for the 1993 and 1994 cruises are almost identical. Both cruises were made during the months of October and show remarkable similar characteristics. Eastward transport is found between leg-3 and leg-1 and westward transport is found between leg-3 and leg-4.

f) In 1995 the eastward transport (still centered between leg-2 and leg-3) has moved southward and is found between leg-2 and leg-4.

Westward transport is now found in the northern part of the region, between leg-1 and leg-2.

g) Most of the transport adjustments made by the least square fit was across leg-2 and leg-3. This result suggests that some part of the coastal transport is not been resolved by the stations along these two legs, but it is showing across leg-1. From figure 2b we know that the stations on leg-1 are closer to the coast than the stations on leg-2 and leg-3. Gulf of Corcovado, located between leg-2 and leg-3 and Gulf "de Penas", located between leg-3 and leg-4 (both shown in figure 1b) have a contribution to the coastal transport that could be estimated around 0.5 Sverdrups.

2.3 WOCE PR-14 Summary and Discussion

2.3.1 Coastal Upwelling and Downwelling

The region of the South East Pacific Ocean overlaid by the WOCE PR-14 cruises can be divided into three regions: a northern region (north of latitude 41° 30' S), a southern region (south of latitude 44° 20' S) and a transition region (centered around latitudes 41° - 44° S).

The northern region is characterized by strong coastal upwelling, low surface salinity and a positive westward horizontal temperature gradient. The low salinity and colder surface waters found near the coast form as a result of the outflow

of fresher water from the Chilean Inland Seas. This surface water is generally known as Modified Sub-Antarctic water (Silva et al, 1995).

The southern region is characterized by a well defined coastal downwelling zone and negative westward horizontal temperature gradient during spring. These characteristics are also present at the end of fall (1995 cruise) but with much less intensity due to the absence of surface heating and a deeper mixed layer. The colder and denser water found in the surface layer comes from the Antarctic Circumpolar Current (ACC) as it enters the sampling region from the west and branches into the Humboldt Current (HC) and the Cape Horn Current (CHC).

The central region or transition region has a coastal zone of weak or moderate or neither upwelling or downwelling region, depending on the season. The position of the South Pacific High (SPH) pressure cell (Figure 19) is responsible for the change in direction of the winds along the coast from ENE to ESE (direction in which the wind blows). The spatial variability of the SPH has been reported by Strub (1996) and Schwerdferger (1976), and depending on its position, the transition region will have an upwelling or downwelling coastal zone. This region has a negative westward horizontal temperature gradient like the southern region due to the presence of the ACC.

2.3.2 Circulation

Combining the results obtained from the potential vorticity maps, the geostrophic velocity fields and water properties, such as salinity and temperature, the following currents have been identified:

26

a) The eastward Antarctic Circumpolar Current (West Wind Drift) entering the north-south transect around latitude 43° S and bifurcating into a strong northward branch and a weak southward branch. The ACC is located in the upper 300 meters of the water column. This current has velocity of 5-9 cm/s, with a maximum of 9-10 cm/s at latitude 43° S, salinity of 33.8-33.9 ‰ and temperature of 9-12.0 °C.

b) The northward branch of the ACC is know as the Humboldt Coastal Current (HCC) and flows in the same general direction of the Humboldt Oceanic Current (Neumann, 1968). The main body of the ACC penetrates to longitude 76° 30' W before turning south to form the HCC. The HCC exists across leg-1 in a northwestward direction at longitude 78° 30' - 79° W.

c) The southward branch of the ACC is known as the Cape Horn Current (CHC) and is farther from the coast than the HCC. The HCC starts to turn south around longitude 80° W and exists across the southernmost leg at longitude 79° W. This current has velocity of 6-9 cm/s.

d) A northward coastal current is seeing in the upper 300 meter layer entering through the eastern (coastal) boundary of the PR-14 region at latitude 42° S. This current is probably the Chile Coastal Current (CCC) defined by Strub (1996) as an "equatorward surface current associated with the coastal upwelling system". This current has

velocity of 5-9 cm/s, salinity of 33.8-34.0 ‰ and temperature of 10-13.5 °C.

e) A southward coastal current, similar to the CCC is found south of latitude 42° S. This current is associated with the coastal downwelling system and has a velocity of 5-10 cm/s, salinity of 33.7-33.8 ‰ and temperature of 10-11 °C. A shallow and narrow layer of fresher and warmer water is found at the surface over this current that has velocities of 10-20 cm/s.

f) A subsurface southward coastal current, located below and to the west of the CCC, in the lower 150-400 meteres, is found in the upper and lower interpolated potential vorticity fields. This current is known as the Gunther Undercurrent (GUC) or Peru-Chile Undercurrent. The GUC has a velocity of 1-3 cm/s, salinity of 34.0-34.4 ‰ and temperature of 8-11 °C.

g) Another southward coastal current, the Peru-Chile Counter Current (PCCC) is found entering leg-1 at longitude 78° W. This current has higher salinity (33.9-34.0‰) and is warmer (9-13.5 °C) than the HCC. It becomes a subsurface currents around latitude 41° 30' S as it moves below the HCC to a depth of 120 meters, surfacing again around latitude 44° 20' S. The PCCC has velocities that range between 1 to 4 cm/s and, it moves in a general southwestward direction exiting at longitude 79° 30' W.

2.3.3 Transport

The net transport into and out of the study region remained almost constant during spring 1993, spring 1994 and fall 1995 (Table 1).

a) The main eastward transport is centered between leg-2 and leg-3 (Figure 2b) with values that range from 3.04 to 3.44 Sverdrups.

b) The northward transport is between 2.58 and 2.95 Sverdrups (71% to 76% of the net eastward transport, respectively).

c) The southward transport is between 0.68 and 0.76 Sverdrups (29% to 24% of the net eastward transport, respectively).

The bifurcation of the Antarctic Circumpolar Current (or the West Wind Drift - WWD) occurs between latitudes 41° 30' S and 44° 20' S. The uncertainty in the location of the bifurcation of the ACC is related to the latitudinal extension of the incoming eastward flow and not to the position of the main axis of the flow (43° S). The latitudinal extension of the ACC, centered around latitude 43° S, is controlled by the seasonal displacement of the SPH. In other words, the direction of the eastward or westward flow in the upper or lower part of the transport box is related to the spatial variability of the location of the SPH pressure cell.

2.3.4 Future Studies

In order to obtain a more accurate description of the temporal and spatial variability of the eastern boundary current system and west wind drift transport the following initiatives should be carried out:

a) Perform two years of seasonal cruises along the same legs of the PR-14 cruises, but with stations that go all the way down to the bottom and close enough to the coast to resolve the "coastal" circulation.

b) Install at least one current-meter array for one year along leg-1 to obtain an absolute velocity reference for the geostrophic velocity calculations.

c) Perform analyses of the water samples collected during the seasonal cruises to obtain one more parameter to better identify the water masses (oxygen, nutrients and radiotracers).

d) Complement this study with other WOCE lines and projects in the area, such as the study of the propagation of the Antartcic Circumpolar Wave (ACW) along the coast of Chile, the P6 hydrographic line, to obtain a more general and comprehensive description of the eastern boundary current system.

3. SOUTH EAST PACIFIC OCEAN NUMERICAL MODEL

3.1 Model Description

The model used in this research is the Naval Research Laboratory global ocean model, best known as the NRL model. The NRL model is a hydrodynamic-isopycnal nonlinear primitive equation, multi-layer ocean circulation model. A detailed-general description of the NRL model is given in Appendix A, as described by Wallcraft (1991).

The model grid for the global ocean model covers the globe from 72°S to 71°N. The horizontal resolution is 1/4°, 0.25° latitude by 0.35° longitude. The subregion used for this research corresponds to the South East Pacific Ocean and goes from latitude 5° S to 55° S and from the west coast of South America to longitude 110° W.

The atmospheric forcing is introduced into the model through realistic wind stress. The model is spun-up from rest to statistical equilibrium using the Hellerman and Rosenstein (1983) monthly mean wind stress climatology. To drive the model on interannual time scales, 1000-mbar winds from the European Centre for Medium-Range Weather Forecast (ECMWF) are used. The ECMWF wind stress data set covers the period from 1981 through 1995.

The ECMWF mean monthly climatology over the 1981-1990 time frame is subtracted from its monthly means and replaced by the Hellerman-Rosenstein annual means. This hybrid wind set is used to extend the integration already spun-up to statistical equilibrium using the Hellerman-Rosenstein monthly winds. Thus, an annual mean solution would still be driven primarily by the Hellerman-Rosenstein data, but seasonal and interannual forcing would come from ECMWF.

Two versions of the model are used:

a) A reduced-gravity version with five active upper layers and, an infinitely deep and at rest lower layer. The model is spun up for 296 model years using the wind stress climatology (smoothed monthly mean winds) and, it is run with daily averaged ECMWF winds starting in 1981. This version of the model is called experiment 6.4 (Exp. 6.4).

b) A six-layer finite-depth version with realistic topography confined to the lowest layer. The wind stress is the same as experiment 6.4, except the spin up is for 227 years. This version of the model is called experiment 7.2 (Exp. 7.2).

Both version have a minimum depth of 200 meters, i.e. the model coastline is defined to coincide with the 200 meter isobath, not the geographical coastline. A summary of layer depth, density of each layer and layer thickness at which to start entrainment or detrainment are given in table 2.

Table 2: Initial layer depths and isopycnal surface depths associated with each layer for the reduced-gravity and finite-depth cases. Layer thickness at which to start entrainment, h_k^+; and a layer thickness at which to start detrainment, h_k^-; are indicated.

		Layer 1	Layer 2	Layer 3	Layer 4	Layer 5	Layer 6
Reduced Gravity Model Exp. 6.4	σ_θ [kg/m3]	24.84	26.00	26.75	27.08	27.34	27.77
	Initial Depth [m]	80	160	160	250	350	∞
	Total depth	*80*	*240*	*400*	*650*	*1000*	∞
	h_k^-	500	600	1200	1200	1200	
	h_k^+	50	40	40	40	40	
Finite Depth Model Exp. 7.2	σ_θ [kg/m3]	25.24	26.47	26.99	27.23	27.39	27.77
	Initial depth [m]	155	185	210	225	225	5500
	Total depth	*155*	*340*	*550*	*775*	*1000*	*6500*
	h_k^-	9999	9999	9999	9999	9999	
	h_k^+	50	40	40	40	40	

3.2 Circulation

The circulation of the South East Pacific ocean will be analyzed in two steps. First, the circulation features found in experiments 6.4 (reduced-gravity) and 7.2 (finite-depth) for the NRL Global Ocean Model Sub-Domain (Figure 1a) will be discussed. Second, the area of the model corresponding to the WOCE PR-14 sampling region (red rectangle in Figure 1a) will be studied and discussed. In both areas, the results of the model for October 1994 will be studied for later comparisons with the result of the flow fields derived from the WOCE PR-14 1994 hydrographic data. The 1984-1994 average flow fields for the months of January-February-March, April-May-June, July-August-September and October-November-December will be analyzed to study the temporal and spatial variability of the circulation.

3.2.1 South East Pacific Ocean

The average October 1994 flow field of the finite-depth model for layer 1 (Figure 24) shows several well organized flow paths that can be identify as:

a) The eastward Antarctic Circumpolar Current (ACC) that meanders around latitude 52° S and flows all the way to the South American coast. Most of the ACC turns north between longitude 91° W and the coast, until it reaches latitude 43° S, where it turns eastward again. The portion of the ACC that keeps going eastward reaches the South American coast and turns south into the Drake Passage becoming the Cape Horn Current (CHC).

b) The northward Humboldt Current (HC) is formed by the ACC after it reaches the coast. The HC bifurcates into two northward branches at latitude 35° S, forming a coastal current known as the Humboldt Coastal Current (HCC) and an offshore current known as the Humboldt Oceanic Current (HOC). The HOC turns toward the west at latitude 25° S, crossing the entire basin and exiting the western boundary of the domain at latitude 20° S. The HCC follows the coastline until it reaches latitude 12° S where it turns toward the west to become the South Equatorial Current (SEC).

c) The CHC formed by the south portion of the ACC at latitude 52°-53° S, flows along the coast into the Drake Passage.

d) The South Pacific Gyre (SPG) is formed by the ACC, the HC and the SEC. The SPG has a zonal extension of about 30 degrees, from latitudes 10° S to 40° S. The east-west axis of the SPG is located around latitude 25° S and it is slightly tilted to the south near the South American coast.

The bottom topography of the NRL Global Ocean model sub-domain is presented in figure 25. Some of the most important features of the topography are labeled on the plot. The effects of the Chile Rise, the Nazca Rise and the Peru-Chile Trench on the currents can be observed in figure 24. The ACC crosses over the Chile Rise at longitude 88° W and then turns toward the east following the 3800 meter isobath. The Peru-Chile Trench helps steer the HCC along the coast until latitude 10° S, where it turns towards the west. The Nazca Rise forces the flow to go south-west until longitude 87° W, where it joints the HOC in its westward motion.

The average October 1994 flow field of the reduced-gravity model for layer 1 (Figure 26) does not present the expected flow patterns known to be found in the South East Pacific Ocean. The ACC does not show a well defined eastward direction and there is no branch of the ACC going into the Drake Passage. The SEC is not joined by an eastern boundary current such as the HC and, between the coast of Peru/Ecuador and longitude 90° W, is poorly defined. A coastal current can be found from latitudes 45° S to 27° S. It is difficult to find the SPG and there is no return flow that could link the SEC with the ACC, at least east of longitude 110° W. Another

35

anomaly of the reduced-gravity model is a very deep layer interface located near the coast of South America, centered around latitude 53° S. This anomaly is due to the strong winds that blow over that part of the ocean and the fact that the absence of bottom topography does not allow the model to limit the deepening of the layer interface.

The results of the two versions of the model (reduced-gravity and finite-depth) show that the bottom topography has a great influence in the general circulation. The fact that bottom topography has a "steering" effect on the currents (as a result of changes of the layer thickness that has to be compensated by changes of the relative vorticity) reveals that the use of a reduced-gravity model to study the circulation over this areas, where there are important topographic features, is inadequate.

To study the spatial and temporal variability of the upper circulation monthly average of flow fields and layer interface depths are used. Each plot corresponds to the average of a three-month period over eleven years (1984-1994). All figures have the same velocity scale and depth color scale to facilitate comparisons. The results are presented for the months of January-February-March (Figure 27), April-May-June (Figure 28), July-August-September (Figure 29) and October-November-December (Figure 30).

The color contours of interface depths show a well defined SPG that extends across the entire basin of the South Pacific Ocean and reaches longitude 75° W at latitude 25° S. In contrast to what was found in figure 24, the SPG has one

overturning cell, centered between latitudes 16° S and 24° S. The double cell structure of figure 24 is filtered out by the time averaging and is not present in any of the four three-month periods. The east-west axis of the SPG is tilted towards the south and goes parallel to the line that links the southern most points of each depth contour. The southeast boundary of the SPG is clearly defined by the geographic location of the southern most section of the Chile Rise and extends towards the west until longitude 89°-90° W, where the flow crosses over a deeper part of the rise (see figure 24). One remarkable feature of these plots is the fact that they all look very much alike with no outstanding differences.

The circulation fields show a SEC that varies slightly in strength and direction, but is always confined along and east-west axis with a maximum southward extension to latitude 16° S. The temporal variability of the SEC is related to the direction and strength of the South East Trade Winds. The maximum strengths are found during Fall season (April-May-June), follow by Winter (July-August-September), Summer (January-February-March) and Spring (October-November-December), in that specific sequence. The HC is stronger during Summer and Spring along the Chilean coast, but it gets weaker and less coherent as it moves along the Peruvian coast, the opposite is true for Winter and Fall months. The latitude at which the HC bifurcates into the HOC and HCC is now locate around 25° S and coincides with the position at which the HC leaves the alongshore path to turn towards the west. The CHC is formed between latitudes 52°-53° S and it is stronger during the months of July-August-September.

37

3.2.2 WOCE PR-14 Sampling Area

The results of the average flow field (October 1994) for the six layers of the finite-depth model of the WOCE PR-14 Sampling Area are presented to describe the circulation and density structure of the region. A plot of bottom topography is also used to study the effects of bathymetry on the circulation.

Figure 31 shows the eastern most section of the Chile Rise located between latitudes 44°-45° S, the alongshore Peru-Chile Trench and a deeper region of 4400-4600 meters at latitude 40° S.

The average flow field in layer 1 (Figure 32) has the ACC coming into the region between latitudes 42°-43° S and moving all the way across the basin until it reaches the eastern boundary and turn towards the north forming the HC. Part of the ACC turns northward and exists across latitude 38° S at longitude 79° W. The flow that comes from the south along the coast joins the ACC and turns towards the east strengthening the ACC. The interface layer depth is shallower south of latitude 42° S (between 45 and 65 meters) and deeper north of latitude 41° S. The largest gradient in interface layer depth follows the gap between the 3600 meter and 4000 meter isobaths at latitude 41°-42° S. This region corresponds to the transition between the shallower northern boundary of the Chile Rise and the deeper central basin.

Layer 2 (Figure 33) is similar to layer 1, but a stronger topographic steering can be seen acting on the currents. The layer interface depth increases from

south to north. The ACC enters at the same latitude, but the southern portion turns to the right along the 3200-3400 meter isobath and then to the left after reaching the shallower region located at 80° W. This portion of the ACC rejoins the main core of the ACC and continues eastward, forming the northward HC. The northern portion of the ACC that exits at longitude 78°-79° W, first turns right over the deeper 4200-4400 meter region and finally turns left (northward) over the shallower 3800-4000 meter region.

Layers 3, 4 and 5 (Figures 34, 35 and 36, respectively), have the deepest layer interface depths in the upper left corner of the region. Two deep "islands" are shown at latitude 40° S and longitude 78° W, and at latitude 38.5°-39° S and longitude 75° W. The flow in these layers tends to loop around the depressions and elevations of the bottom topography and to follow the east-west 3800 meter isobath located at latitude 42° S. Most of the weak flow that is coming across the southern boundary loops around the topographic features of the Chile Rise, and exits towards the west between latitudes 46° S and 48° S without joining the eastward 42° S flow. The flow that enters at latitude 41°-42° S follows a path similar to the one described for the northern portion of the ACC in layer 2, but it follows much more closely the bottom topography of that region.

The lowest layer (layer 6) has a velocity scale factor 4 times larger than the one used in layers 1 and 2, i.e. the largest arrows on the plot correspond to velocities of less than 2 cm/s. The color contour does not represent the interface layer

depth, it is the depth of the lowest layer that has a constant density of 27.77 kg/m^3. The contours of bottom topography (Figure 31) and layer 6 depth (Figure 37) are almost identical, but in figure 37 are smoother, as expected due to the interpolated version of the topography input to the model. The flow is mainly driven by the topographic steering with three well defined loop currents; over the shallower portion of the Chile Rise (dextrogyrous loop); and over the two deeper "islands" of the northern region (levogyrous loops). Layer 6 is the only one that has some kind of southward current alongshore that follows the Peru-Chile Trench.

To study the spatial and temporal variability of the upper circulation in the WOCE PR-14 Sampling Region, monthly average of flow fields and layer interface depths are calculated. The figures correspond to the average of three-month periods over eleven years (1984-1994). All figures have the same velocity scale and depth color scale to facilitate comparisons. The results are presented for the months of January-February-March (Figure 38), April-May-June (Figure 39), July-August-September (Figure 40) and October-November-December (Figure 41).

An important common feature of these plots is that the largest gradient in interface layer depth follows the east-west 3600 meter isobath located at latitude 42° S. At the same time, the ACC enters the WOCE PR-14 Sampling Region parallel to these contours and follows the curvature of them until it exits toward the north as the HC. The combined analysis of the topographic features shown in figures 25 and 31 and the flow fields of figures 27 through 30 indicates that the ACC follows the

northern boundary of the Chile Rise as it moves toward the east and enters the WOCE PR-14 Sampling Region.

The location of the northward turning point of the ACC shifts seasonally from longitude 75° 45' W in October-November-December (OND), to longitude 76° 30' W in January-February-March (JFM), to longitude 77° W in April-May-June (AMJ) and to longitude 78° W in July-August-September (JAS). The exiting latitude of the HC from the WOCE PR-14 Sampling Region varies accordingly with the location of the turning point. In JFM, AMJ and JAS the shape of the curvature of the northward HC follows, more or less, the bottom bathymetry. In OND, when the winds are weaker and the northward coastal current is stronger, the shape of the curvature is modified by coastal upwelling (shallower interface depth along the coast) and strong coastal currents. OND and JFM have upwelling along the coast and a well defined northward coastal current. In JAS the coast has upwelling north of latitude 44° S and downwelling south of this latitude. The downwelling in layer 1 is compensated by upwelling of the interface depth between layers 2 and 3, resulting in a northward current in the upper layer. AMJ has a southward current alongshore, south of latitude 40° S, that is related to coastal downwelling.

3.3 Transport

Transport calculations were done using the layer velocities and the

layer thickness obtained from the reduced-gravity and finite-depth models. Each grid point has a different velocity value, but because these are layer models the velocity is constant within each layer. The results correspond to the vertically integrated transport of the upper 5 layers. The transports were averaged over a time-period equivalent to the length of the WOCE PR-14 cruises of 1994 and 1995. The transport was calculated at the same locations indicated in figure 23, with the following exceptions:

a) The eastern most station of each of the east-west legs was chosen to be the first grid point of the model, so only the flow between the 200 meter isobath and the coast was not considered.

b) Side III of figure 23 was calculated along latitude 44° 30' S, instead of 44° 20' S.

c) The reference level was set to be at the interface depth between layers 5 and 6 in the finite-depth model and between layer 5 and the infinitely deep lower layer in the reduced-gravity model. For example, the interface layer depth in the finite-depth model in October 1994 was between 1100 and 1210 meters.

The results of the average vertically integrated transport for October 1994 and May/June 1995 are presented in table 3. The definition of the boxes and sides is in figure 23, with the exceptions described in letters a), b) and c), listed above.

Table 3: Average vertically Integrated Transport (upper 5 layers) obtained from the output of the Naval Research Laboratory (NRL) model. Exp. 7.2 = finite-depth model, exp. 6.4 = reduced-gravity model. Transport is given in Sverdrups [Sv]. 1 Sv = 10^6 m³/s. Arrows after transport values indicate direction of the flow. ↑ = Northward, ↓ = Southward, → = Eastward and ← = Westward. Shaded cells are used to highlight each transport box.

		Exp. 7.2 October 1994 [Sverdrups]	Exp. 7.2 May/June 1995 [Sverdrups]	Exp. 6.4 October 1994 [Sverdrups]	Exp. 6.4 May/June 1995 [Sverdrups]
Box 1	38°00'S	4.73 ↑	12.71 ↑	7.01 ↑	13.16 ↑
Box 1	Side V	0.72 ←	4.54 →	0.40 →	4.49 →
Box 1 | Box 2	41°30'S	5.54 ↑	7.29 ↑	3.02 ↑	7.39 ↑
Box 2	Side VI	7.09 →	4.33 →	5.16 →	7.19 →
Box 2 | Box 3	44°30'S	0.30 ↓	2.54 ↑	0.21 ↑	0.70 ↓
Box 3	Side VII	0.44 →	1.48 →	0.25 →	0.92 ←
Box 3	48°00'S	0.67 ↓	1.01 ↑	0.24 ↓	0.23 ↓
Net Transport across long. 080° 44' W	Side V + VI + VII	6.81 →	10.67 →	5.81 →	10.76 →

Some of the most important characteristics of the transport are (Table 3):

a) In both experiments the largest part of the eastward transport comes into the region between latitudes 41° 30' S and 44° 30' S.

b) In experiment 7.2 in 1994 the zonal transport is towards the east in box 2 and box 3 and towards the west in box 1. The zonal transport in boxes 1 and 3 is much smaller than in box 2. The lateral zonal transport is formed by a small recirculation

of the ACC towards the west (box 1) and by the combination of a northward current that enters box 3 across latitude 48° S and turns westward and the remaining part of the ACC that enters box 3 through side VII.

c) The meridional transport in experiment 7.2 in 1994 is towards the north across latitudes 38° S and 41° 30' S and towards the south across latitudes 44° 30' S and 48° S. The meridional transport if formed by the bifurcation of the ACC and by a coastal current that sometimes joins the ACC at the bifurcation point. The southward transport is generated by a few weak currents present in layers 2 and 3 that are topographically steered over and north of the Chile Rise and do not form a coherent southward current that could be traced outside the WOCE PR-14 Sampling Region.

d) Experiment 6.4 in 1994 gives similar qualitative results for the zonal transport, but the meridional transport is too large across latitude 38° S.

e) The results of both experiments in 1995 give extremely high values of transport along the western and northern sides of the outside box. These results are consistent with the flow fields obtained for the year 1995 and are related to abnormally high ECMWF wind values in 1995. These results will be regarded as wrong, until the input wind fields can be verified with ECMWF.

3.4 NRL Model Summary and Discussion

The NRL finite-depth model has proven to be a valuable tool in the study of temporal and spatial variability of the eastern boundary current system of the South East Pacific Ocean. The knowledge that bottom topography has a considerable

steering effect on the currents of the region is important for the understanding of some of the main features of the flow described in this chapter.

The NRL model does not reproduce the near shore transport, nor the Gunther Undercurrent (GUC). The lack of accuracy along the coast is assumed to be a result of not having open-boundary sections that could simulate the flow of fresher and colder water from the Chilean Inland Seas into the Pacific Ocean. These fluxes are not known, but they are being measured as part of the Chilean Inland Seas Experiment .

The CHC is formed (in experiment 7.2) at a higher latitude by the portion of the ACC that does not cross over the Chile Rise and impinges the coast turning south into the Drake Passage. The actual CHC should move southward along the coast, formed by the bifurcation of the ACC around latitude 42° S, and joined by the south portion of the ACC at latitude 53° S.

The fact that the ACC enters the WOCE PR-14 Sampling Region around latitude 42° S year round, following the east-west 3600 meter isobath, is a very important result. The meridional extension of the ACC across longitude 80° 40' W is controlled by local winds generated by the interaction of the South Pacific High (SPH) pressure center and the Amundsen Sea Low pressure center. The winds change the magnitude and direction of the east-west transport in boxes 1 and 3 (figure 23) - lateral transports associated with the ACC transport - creating the impression that the ACC has moved southward or northward, while in reality the main flow has always been centered at 42°-43°S.

Another conclusion from the results of experiment 7.2 is the fact that the turning point of the ACC is related to the circulation and density structure induced by winds in the northern part of the WOCE PR-14 Sampling Region (north of latitude 42° S). Several authors had documented the change in position of the center of the SPH from Summer to Winter (Strub et al., 1996; Schwerdtfeger, 1976). In Winter (June-July-August) the SPH moves about 5 degrees of latitude northwest of the Summer position, diminishing the effect of the anticyclonic winds on the northern portion of the WOCE PR-14 Sampling Region. The variability in the intensity of the winds in the northern part of the region changes the depth of the mixed layer and therefore, the vertical density structure. Figures 39 through 41 show the temporal variability of the vertical structure in the northern part of the WOCE PR-14 Sampling Region. Figure 40 is the result of the SPH at its northern most position; as it moves southeastward to its summer location the upper layer thickness increases (Figure 41) and the deepening effect moves southward; when the SPH reaches its southern most location the layer thickness is maximum and the deepening effect stops moving southward (Figure 39); finally, when the SPH starts retrieving northwestward the layer thickness starts decreasing.

4. CONCLUSIONS AND SUMMARY

4.1 Conclusions

4.1.1 Circulation

The results are obtained from the analysis of the hydrographic data collected during Spring of 1993 and 1994 and Winter of 1995, in conjunction with the results of the NRL finite-depth model. Considerable new knowledge is gained. All the following features of the South East Pacific Ocean circulation are now understood, identified and described:

- The eastward Antarctic Circumpolar Current (West Wind Drift): a current that moves eastward along the northern boundary of the Chile Rise and reaches the coast of Chile at latitude 42°-43° S. The ACC bifurcates into a strong northward branch and a weak southward branch. The northward branch is know as the Humboldt Current and the southward branch as the Cape Horn Current. The ACC travels in the upper 300 meters of the water column and it is characterized by an average velocity of 5-9 cm/s, salinity of 33.8-33.9 ‰ and temperature of 9-12° C. The location of the bifurcation has been found to be centered between latitudes 42° and 43° S. The position of the main flow is constant, but the meridional extension

of the current (i.e. north-south width) changes seasonally, adding a lateral flow to the south or north of the main axis, giving the impression that the ACC has moved southward or northward. Using the NRL model the temporal and spatial variability of the turning point (location where the ACC turns toward the north to become the HC) has been linked to the position of the SPH and therefore, to the density structure induced by winds in the northern portion of the WOCE PR-14 Sampling Region.

- The HC flows northward along the Chilean coast until latitude 25° S, where it splits into two branches. A coastal branch known as the HCC that continues along the coast until latitude 8-15° S where it turns west to join the SPG. An oceanic branch known as the HOC that leaves the coast in a general northwest direction joining the SPG as its travels westward.

- The CHC, southward branch of the ACC bifurcation, exiting the WOCE PR-14 Sampling Region at longitude 79° W and flowing towards the Drake Passage in a general direction parallel to the coast. The HCC is reinforced by a small branch of the ACC that reaches the South American coast at latitude 52°-53° S and turns southward into the Drake Passage.

- A subsurface southward coastal current, the Gunther Undercurrent, was found in the lower 150-400 meters, west of the locally induced coastal upwelling and downwelling currents. The GUC has a velocity of 1-3 cm/s, salinity of 34.0-34.4 ‰ and temperature of 8-11° C.

- The Peru-Chile Counter Current is found at longitude 78° W and latitude 38° S. This current has higher salinity (33.9-34.0‰) and is warmer (9-13.5 °C) than the HCC. It becomes a subsurface currents around latitude 41° 30' S as it moves below the HCC to a depth of 120 meters, surfacing again around latitude 44° 20' S. The PCCC has velocities that range between 1 to 4 cm/s and, it moves in a general southwestward direction.

4.1.2 Transport

The net transport into and out of the WOCE PR-14 Sampling Region remained almost constant during spring 1993, spring 1994 and fall 1995. The main eastward transport is centered between latitudes 42°-43° S with values that range from 3.04 to 3.44 Sverdrups. The northward transport across latitude 38° S is between 2.58 and 2.95 Sverdrups (71% to 76% of the net eastward transport, respectively). The southward transport across latitude 48° S is between 0.68 and 0.76 Sverdrups (29% to 24% of the net eastward transport, respectively).

The transport calculations required more hydrographic stations near the coast along the east-west legs of the cruise to better resolve the coastal circulation and to include the flow contribution of the Chilean Inland Seas.

As a preliminary result, the eastward transport obtained from the hydrographic data is almost constant.

4.2 Summary

The NRL finite-depth model has proven to be a valuable tool in the study of temporal and spatial variability of the eastern boundary current system of the South East Pacific Ocean. The knowledge that bottom topography has a considerable steering effect on the currents of the region is important for the understanding of some of the main features of the South Pacific Eastern Boundary System.

The results of this study show that the two goals of the World Ocean Circulation Experiment PR-14 cruise have been achieved. A useful description of the ocean behavior of the transition zone (circulation and transport) has been made using the data collected during 1993, 1994 and 1995. The location of the bifurcation of the ACC has been found and some of the physical processes involved have been described and studied.

Future studies, involving the use of data collected in several international cruises and experiments in the South East Pacific Ocean, complemented with numerical models, will make possible to describe and analyze the large scale and mesoscale variability of the eastern boundary current system.

APPENDIX A

THE NAVY LAYER OCEAN MODEL

1. ACKNOWLEDGMENTS

The general description of the Navy Layered Ocean Model (known as NRL model) is based on the Naval Oceanographic and Atmospheric Research Laboratory (NOARL) Report 35 *"The Navy Layered Ocean Model Users Guide"* prepared for The Ocean Science and Prediction Division by A. J. Wallcraft in 1991, as part of contract # N00014-89-C-6002. Minor modifications were made to section 3, "Model Parameters", to describe the case studied in this research.

2. THE NRL MODEL

2.1 Introduction

The NRL model was originally written by H. Hurlburt and D. Thompson in 1980 and used to study the Gulf of Mexico. The first version was a one- or two-layer finite depth, or one-active-layer reduced-gravity, hydrodynamic primitive

equation ocean model on a beta-plane. It had a free surface and used a semi-implicit time scheme formulated on a Arakawa C-grid, and could handle only rectangular or simple non-rectangular regions.

Since 1980, the NRL model has been greatly expanded and now includes the following major features and improvements:

Any number of layers in the vertical.

a) Nonlinear primitive equations.

b) Free surface.

c) Semi-implicit time scheme.

d) Hydrodynamic, i.e., isopycnal.

e) Full-scale bottom topography in lowest layer.

f) Arbitrary coastline.

g) Solves any closed geometry with no limits to the number of islands.

h) The grid is uniform, but it can be on a beta-plane, on a f-plane, or on a surface of an earth-sized sphere. It allows different resolutions down to 1/64° (limited by computer resources).

i) Versions of the reduced-gravity models that use an explicit time scheme are available.

j) Open outflow boundaries use a variant of the Orlanski (1976) radiation condition, developed by Heburn (1986).

k) Variable (any) number of open-boundary sections can be placed along any zonal or meridional sections of the model closed

geometry, and each layer can have its own set of open boundary conditions.

l) To control the surfacing of layer interfaces (i.e. outcrop of the upper layer) a process called "hydromixing" is used. This process is identical to mixing in a thermodynamical layered model, except that layer density is kept constant.

m) Allows longer time steps than primitive equation models that use a rigid lid or time splitting (advantage of using a semi-implicit time scheme).

The major disadvantage of this layer formulation is that bottom topography is confined to the lowest layer, which makes the model less useful in coastal regions and in any coastal region with depths of less than 200 meters (isobath of minimum depth in the NRL model). However, it has proved quite successful at modeling seamounts, e.g.., the effect of the New England seamount chain on the Gulf Stream (Hurlburt and Thompson, 1984).

2.2 Model Equations

The vertically integrated equations of motion used in the n-layer finite depth hydrodynamical model are, for k=1,..., n:

$$\frac{\partial \vec{V}_k}{\partial t} + \left(\nabla \cdot \vec{V}_k + \vec{V}_k \cdot \nabla\right)\vec{v}_k + \hat{k} \times f\vec{V}_k = -h_k \sum_{l=1}^{n} G_{kl} \nabla\left(h_l - H_l\right)$$

$$+ \max\left(0, \omega_k\right)\vec{v}_{k+1} - \left(\max\left(0, -\omega_k\right) + \max\left(0, \omega_{k-1}\right)\right)\vec{v}_k +$$

$$\max\left(0, -\omega_{k-1}\right)\vec{v}_{k-1} + \frac{\left(\vec{\tau}_{k-1} - \vec{\tau}_k\right)}{\rho_0} + A_H h_k \nabla^2 \vec{v}_k \qquad \text{(A.1)}$$

$$\frac{\partial h_k}{\partial t} + \nabla \cdot \vec{V}_k = \omega_k - \omega_{k-1}$$

where:

$h_k = k-\text{th layer thickness}$

$\vec{v}_k = k-\text{th layer velocity}$

$\vec{V}_k = h_k \vec{v}_k = k-\text{th layer transport}$

$H_k = k-\text{th layer thickness at rest}$

$H_n = D(x, y) - \sum_{l=1}^{n-1} H_l$

$D(x, y) = \text{total ocean depth at rest}$

$\rho_k = k-\text{th layer density, constant in space and time}$

$$G_{kl} = \begin{cases} g & \text{for } 1 \leq k \\ g - g\left(\dfrac{\rho_l - \rho_k}{\rho_0}\right) & \text{for } 1 > k \end{cases}$$

$f = \text{coriolis parameter}$

$A_H = \text{coefficient of horizontal eddy viscosity}$

$C_k = \text{coefficient of interfacial friction}$

$C_b = \text{coefficient of bottom friction}$

$\vec{\tau}_w = \text{wind stress}$

$$\vec{\tau}_k = \begin{cases} \vec{\tau}_w & \text{for } k = 0 \\ C_k \rho_0 \left|\vec{v}_k - \vec{v}_{k+1}\right|\left(\vec{v}_k - \vec{v}_{k+1}\right) & \text{for } k = 1, \ldots, n-1 \\ C_b \rho_0 \left|\vec{v}_n\right|\vec{v}_n & \text{for } k = n \end{cases}$$

$$\omega_k = \begin{cases} 0 & \text{for } k = 0, n \\ \max\left(0, \omega_k^+\right) - \max\left(0, \omega_k^-\right) - h_k \hat{\omega}_k & \text{for } k = 1, \ldots, n-1 \end{cases}$$

$$\omega^+_k = \widetilde{\omega}_k \frac{h^+_k}{4} \left(\frac{1}{h_k} - \frac{1}{h^+_k} \right)$$

$$\omega^-_k = \widetilde{\omega}_k \frac{h^+_k}{4} \left(\frac{1}{h^-_k + h^+_k - h_k} - \frac{1}{h^+_k} \right)$$

$$\widetilde{\omega}_k = \frac{\iint \left(\max(0, \omega^+_k) - \max(0, \omega^-_k) \right)}{\iint H_k}$$

$\widetilde{\omega}_k = k - $th interface reference vertical mixing velocity

$h^+_k = k - $th layer thickness at which entrainment starts

$h^-_k = k - $th layer thickness at which detrainment starts

This layered formulation, that uses the transport as a dependent variable, handles strongly sloping topography, especially well, as long as it is confined to the lowest layer. The bottom topography appears multiplicatively in the pressure gradient term, and is differentiated only to the extent that it affects the velocity field in the advective terms. When large-amplitude topography is introduced, restrictions on the time step and the eddy coefficient are affected only to the extent that the topography determines the amplitude of the velocity field. Another advantage of this formulation is that the continuity equation written in transport form becomes linear, thus avoiding complications from the nonlinear advective term when layer thickness and velocity are used as variables.

This hydrodynamical model is an isopycnal model (the density is constant in space and time for each layer), but, hydromixing is allowed to prevent surfacing. The fluid entrained from another layer is assumed to be at the same density as the receiving layer. It is primarily designed to prevent any layer interface from surfacing, and depends only on the layer thickness and three user supplied parameters:

a reference vertical mixing velocity, $\widetilde{\omega}_k$; a layer thickness at which to start the entrainment, h_k^+; and a layer thickness at which to start the detrainment, h_k^-.

In practice explicit detrainment is often deactivated by making h_k^- very deep. Mixing has been formulated to involve no net transfer of fluid between layers, so if there is local entrainment it will balance throughout the whole domain by detrainment. The global mixing balance term, $\hat{\omega}_k$, has been included to allow long-term integrations; however it is an additional source of damping. For region with port forcing or river discharge, the layer thickness can alternately be balanced by adjusting the net transport in and out of he region, thus removing the need for the $\hat{\omega}_k$ term.

The reduced-gravity version of the hydrodynamical model with n active layers has the lowest layer that is infinitely deep and at rest, i.e., $\vec{V}_{n+1} = 0$, $h_{n+1} = \infty$, and $\nabla h_{n+1} = 0$. The equations for the reduced-gravity model are the same as in the case for the n-layer hydrodynamical finite depth model, except that:

$$H_n = \text{constant}$$

$$G_{kl} = \begin{cases} g\dfrac{\left(\rho_{n+1} - \rho_k\right)}{\rho_0} & \text{for } l \le k \\[4mm] g\dfrac{\left(\rho_{n+1} - \rho_l\right)}{\rho_0} & \text{for } l > k \end{cases}$$

$$\vec{\tau}_k = \begin{cases} \vec{\tau}_w & \text{for } k = 0 \\[2mm] C_k\rho_0\left|\vec{v}_k - \vec{v}_{k+1}\right|\left(\vec{v}_k - \vec{v}_{k+1}\right) & \text{for } k = 1,\ldots,n \end{cases}$$

$$\omega_k = \begin{cases} 0 & \text{for } k = 0 \\[2mm] \max\left(0,\omega_k^+\right) - \max\left(0,\omega_k^-\right) - h_k\hat{\omega}_k & \text{for } k = 1,\ldots,n \end{cases}$$

In general, the reduced-gravity version of the NRL model is more robust than the finite-depth version, and an n-1 active-layer reduced-gravity model can give similar results to an n-layer finite depth model. So it is often cost effective to develop a reduced-gravity model of a region first and then go on to a finite depth model.

2.3 Finite Difference Equations

The model equations are solved numerically on a staggered C-grid to save disk space and computation time. The following equations deal with the beta-plane version of the model. The operators are defined as:

$$
\delta_{mz}\left(W(z)\right) = \left(m\Delta\right)^{-1}\left[W\left(z + \frac{m\Delta}{2}\right) - W\left(z - \frac{m\Delta}{2}\right)\right]
$$
$$
\overline{W(z)}mz = \frac{1}{2}\left[W\left(z + \frac{m\Delta}{2}\right) + W\left(z - \frac{m\Delta}{2}\right)\right]
$$
(A.2)

where W is a function of the discrete variable z, Δ refers to a space or time increment, and m is an integer assumed to be 1 if omitted.

Now using this operators we can write the finite difference form of the finite depth hydrodynamics model equations for k=1,..,n as:

$$\delta_{2t}U = -\delta_x\left(\overline{U}^x\overline{u}^x\right) - \delta_y\left(\overline{V}^x\overline{u}^y\right) + \overline{\left(f\,\overline{v}^y h\right)}^x$$

$$-\overline{h}^x\sum_{l=1}^n G_{kl}\delta_x(h_l - H_l) - \hat{H}_k\sum_{l=1}^n G_{kl}\delta_x\left(\overline{(h_l - H_l)}^{2t} - (h_l - H_l)\right)$$

$$+\max\left(0, -\overline{\omega}^x_{k-1}\right)u^{t-\Delta t}_{k+1} - \left(\max\left(0, -\overline{\omega}^x_k\right) + \max\left(0, \overline{\omega}^x_{k-1}\right)\right)u^{t-\Delta t}_k \qquad (A.3)$$

$$+\max\left(0, -\overline{\omega}^x_{k-1}\right)u^{t-\Delta t}_{k-1} + \frac{\left(\tau^x_{k-1} - \tau^x_k\right)}{\rho_0}$$

$$+A_H\overline{h^{t-\Delta t}}^x\left(\delta_x\delta_x u^{t-\Delta t} + \delta_y\delta_y u^{t-\Delta t}\right)$$

$$\delta_{2t}V = -\delta_x\left(\overline{U}^y\overline{v}^x\right) - \delta_y\left(\overline{V}^y\overline{v}^y\right) - \overline{\left(f\,\overline{u}^x h\right)}^y$$

$$-\overline{h}^y\sum_{l=1}^n\left(G_{kl}\delta_y(h_l - H_l)\right) - \hat{H}_k\sum_{l=1}^n G_{kl}\delta_y\left(\overline{(h_l - H_l)}^{2t} - (h_l - H_l)\right)$$

$$+\max\left(0, \overline{\omega}^y_k\right)v^{t-\Delta t}_{k+1} - \left(\max\left(0, -\overline{\omega}^y_k\right) + \max\left(0, \overline{\omega}^y_{k-1}\right)\right)v^{t-\Delta t}_k \qquad (A.4)$$

$$+\max\left(0, \overline{\omega}^y_{k-1}\right)v^{t-\Delta t}_{k-1} + \frac{\left(\tau^y_{k-1} - \tau^y_k\right)}{\rho_0}$$

$$+A_H\overline{h^{t-\Delta t}}^y\left(\delta_x\delta_x v^{t-\Delta t} + \delta_y\delta_y v^{t-\Delta t}\right)$$

$$\delta_{2t}h = -\delta_x\left(\overline{U}^{2t}\right) - \delta_y\left(\overline{V}^{2t}\right) + \omega_k - \omega_{k-1} \qquad (A.5)$$

$$\omega = \begin{cases} 0 & \text{for } k = 0, n \\ \max(0, \omega^+) - \max(0, \omega^-) - h_k\hat{\omega} & \text{for } k = 1,..,n-1 \end{cases} \qquad (A.6)$$

$$\omega^+ = q\frac{h^+}{4}\left(\frac{1}{h^{t-\Delta t}} - \frac{1}{h^+}\right) \qquad (A.7)$$

$$\omega^- = q\frac{h^+}{4}\left(\frac{1}{h^- + h^+ - h^{t-\Delta t}} - \frac{1}{h^+}\right) \qquad (A.8)$$

$$\hat{\omega}_k = \frac{\iint\left(\max(0, \omega^+) - \max(0, \omega^-)\right)}{\iint H_k} \qquad (A.9)$$

$$\Delta u = u_k^{t-\Delta t} - u_{k+1}^{t-\Delta t} \tag{A.10}$$

$$\Delta v = v_k^{t-\Delta t} - v_{k+1}^{t-\Delta t} \tag{A.11}$$

$$
\tau_k^x =
\begin{cases}
\tau_w^x & \text{for } k = 0 \\[2ex]
C_k \rho_0 \Delta u \sqrt{(\Delta u)^2 + \left(\overline{\left(\overline{(\Delta v)^y} \right)^x} \right)^2} & \text{for } k = 1, \ldots, n-1 \\[3ex]
C_b \rho_0 u^{t-\Delta t} \sqrt{\left(u^{t-\Delta t} \right)^2 + \left(\overline{\left(\overline{\left(v^{t-\Delta t} \right)^y} \right)^x} \right)^2} & \text{for } k = n
\end{cases}
\tag{A.12}
$$

$$
\tau_k^y =
\begin{cases}
\tau_w^y & \text{for } k = 0 \\[2ex]
C_k \rho_0 \Delta v \sqrt{(\Delta v)^2 + \left(\overline{\left(\overline{(\Delta u)^x} \right)^y} \right)^2} & \text{for } k = 1, \ldots, n-1 \\[3ex]
C_b \rho_0 v^{t-\Delta t} \sqrt{\left(v^{t-\Delta t} \right)^2 + \left(\overline{\left(\overline{\left(u^{t-\Delta t} \right)^x} \right)^y} \right)^2} & \text{for } k = n
\end{cases}
\tag{A.13}
$$

The only two terms that have been made implicit are the pressure-gradient term in the momentum equation and the mass-divergence term in the continuity equation. i.e. this is a semi-implicit formulation of the equations that treats the linear part of the gravity waves implicitly. It is unconditionally stable, provided the constant $\hat{H}_k$ are such that the explicit part of the pressure-gradient term always acts to slow the gravity waves. The model requires $\hat{H}_k$ to be greater than h_k, which guarantees unconditional stability.

The linear CFL limit on the time step is :

$$\Delta t \leq \sqrt{\left(\frac{u_{max}}{\Delta x}\right)^2 + \left(\frac{v_{max}}{\Delta y}\right)^2 + f^2} \tag{A.14}$$

and the time step used in actual runs of the model is between 90% to 95% of this limit.

Expressing the n-continuity equations, one for each layer, as a single n-element vector equation, we obtain:

$$\begin{bmatrix} h_1^{t+\Delta t} \\ \vdots \\ h_n^{t+\Delta t} \end{bmatrix} = \begin{bmatrix} h_1^* \\ \vdots \\ h_n^* \end{bmatrix} + (\Delta t)^2 \begin{bmatrix} \hat{H}_1 & & \\ & \ddots & \\ & & \hat{H}_n \end{bmatrix} G \begin{bmatrix} \delta^2 & & \\ & \ddots & \\ & & \delta^2 \end{bmatrix} \begin{bmatrix} h_1^{t+\Delta t} \\ \vdots \\ h_n^{t+\Delta t} \end{bmatrix} \tag{A.15}$$

where $\delta^2 = \delta_x \delta_x + \delta_y \delta_y$, and h_k^* contains all terms at time levels t and t-Δt.

Now, a real eigenmatrix X and eigenvalues λ_k^2 exist, such that

$$\begin{bmatrix} \hat{H}_1 & & \\ & \ddots & \\ & & \hat{H}_n \end{bmatrix} G = \begin{bmatrix} \lambda_1^2 & & \\ & \ddots & \\ & & \lambda_n^2 \end{bmatrix} X^{-1} \tag{A.16}$$

So,

$$\begin{bmatrix} \delta^2 - 1/(\lambda_1 \Delta t)^2 & & \\ & \ddots & \\ & & \delta^2 - 1/(\lambda_n \Delta t)^2 \end{bmatrix} \begin{bmatrix} \tilde{h}_1 \\ \vdots \\ \tilde{h}_n \end{bmatrix} = -X^{-1} \begin{bmatrix} h_1^* \\ \vdots \\ h_n^* \end{bmatrix} \tag{A.17}$$

$$\begin{bmatrix} h_1^{t+\Delta t} \\ \vdots \\ h_n^{t+\Delta t} \end{bmatrix} = -X^{-1} \begin{bmatrix} \tilde{h}_1 \\ \vdots \\ \tilde{h}_n \end{bmatrix} \tag{A.18}$$

The semi-implicit continuity equation in real space consists of n-coupled elliptical partial differential equations. When these equations are converted to

60

modal space, they are decoupled into n-independent two-dimensional Helmoltz equations. The decoupling gives rise to Helmholtz equations because $\hat{H}_k$ and G_{kl} (and, therefore X and λ_k) are constants.

The time differencing scheme is leapfrog, but a Heun predictor-corrector difference (Roache, 1976) is used to start and restart. Every so often, the solution for at least three adjacent time steps is averaged to exactly filter $2\Delta t$ time splitting, and the model is restarted.

2.4 Boundary Conditions

On the C-grid: zonal boundary sections pass through V grid points, meridional sections pass through U grid points and any diagonal boundary sections pass through U and V points. Because of the distribution of U,V and h on a C-grid, in all cases the boundary is exactly one-half the distance of an increment in x or y, from the nearest h grid point. So the coast is uniquely defined by a map indicating which h grid nodes are sea and which are land.

The walls are rigid and no-slip condition is prescribed on the tangential flow, with the exception of inflow and outflow at boundary ports. These boundary conditions are implemented in the model by setting all velocity and transport components that lie on the boundary to zero, and setting all components that lie one-half grid spacing on the land side of the boundary to minus those that are one-half grid spacing in the sea side of the boundary (inverse reflection). If a U land point has U sea points directly to its north and south, or if a V land point has V sea points directly to

its west or east, then the boundary must pass through a land point. At a port setup for inflow only, the transport $\vec{V}_k$, or the velocity $\vec{v}_k$, are external forcing fields. The flow at a port setup for outflow is predicted in three steps.

First, a modified Orlanski (1976) radiation condition is used. Consider, for example, a port on the northern boundary of the region. Then, for each component of transport,

$$q_B^{t+\Delta t} = \frac{\left(\left(1 - \dfrac{c\Delta t}{\Delta y}\right)q_B^{t-\Delta t} + \dfrac{2c\Delta t}{\Delta y}q_B^t - 1\right)}{\left(1 + \dfrac{c\Delta t}{\Delta y}\right)} \tag{A.19}$$

$$c = \min\left(\Delta y / \Delta t, \ \max\left(c_k, \bar{v}_k\right)\right)$$

where B refers to the outflow boundary and B-1 to one grid point interior to the boundary, $\bar{v}_k$ is a reference outflow speed that is usually set to the average inflow speed at the inflow ports, and the phase speed, c_k is determined locally for each wave mode. There are several ways to determine the local phase speed, c_k, but the simplest scheme, with $c_k = \bar{v}_k$, is often very effective. Overall, this boundary condition always moves information from the interior toward, and normal to, the open boundary.

Second, a linear implicit drag is an option that may be applied at all points on the port where inflow is predicted. This option prevents the development of any unrealistically large recirculation at the open boundary by applying a "brake" on the inflow component of the recirculation. The e-folding time scale of the drag is chosen to be sufficiently long to allow waves and eddies to migrate out of the region.

Third, the velocity across each outflow port in the a layer is uniformly increased or decreased such that the total inflow mass transport, from all inflow ports in that layer, is matched by the total outflow mass transport. This hard mass constraint, time step by time step, on inflow and outflow does not allow for temporary mass storage in the region, and it can lead to problems when spinning up a model from rest. However, it allows the use of excess mass as a debugging tool (since there should not be any net exchange in mass with this scheme).

To solve the Helmholtz equations for h, we require boundary values for U and V at the new time level. Since interior U and V are not available until after the new h is known, some boundary conditions on U and V that involve interior values at the new time level could not be used in a semi-implicit model. However, simple boundary conditions of this form, such as those at a free-slip boundary, do not cause any difficulty. In the present model at a solid, no-slip boundary, U and V are both zero for all time; at an inflow port, they are prescribed; and at an outflow port, they depend on interior values from previous time steps only. So in all cases the required boundary values are available when the Helmholtz equation is solved . Note that the value of h cannot be prescribed at an open boundary in this model.

2.5 External Forcing Input

The allowed external forcing fields for the model are bathymetry, wind stress, and inflow boundary, velocity or transport. All these fields are optional, except for bathymetry, are optional and can be omitted from a given model run.

Bathymetry is defined on the same grid as h, and it is usually read-in from a file at the beginning of the model run. It must be sufficiently deep to be always below the lowest layer interface, but is otherwise arbitrary. However, it is advisable to smooth out any $2\Delta x$ or $2\Delta y$ components that are present before using a bathymetry field in the model. The bathymetry is also used to define the model coastline. If a point has a positive bathymetric value, then is taken as sea; otherwise, it is a land point. Any land-sea geometry is allowed; there is no limit on the number of islands in the geometry, and single-point islands are allowed. Since the bathymetry file also defines the coastline, it must be present. However, in reduced gravity models it has no other effect, and in finite-depth models the amplitude of the topography can be specified. An amplitude of zero corresponds to a flat-bottom case, and an amplitude of one corresponds to the topography exactly as input. Any amplitude may be used, but typically the bathymetry might be defined to reach the surface, and an amplitude slightly less than one would be used to ensure that the actual model bathymetry always remained below the lowest interface.

The wind stress are defined on the U and V grid points. Wind stresses are usually read-in from a file, or files, during the model run. The time intervals between wind input are arbitrary and can change from one wind record to the next. At any given time step the model wind stress is formed by a linear interpolation of the nearest input wind stress before that time and the nearest input wind stress after that time. Since the scale of wind features is usually far larger than the scale of oceanic features, only one of every two wind stress values is input and saved in each direction.

64

i.e., only one-fourth of the points are in the wind-stress file. The wind-stress values at the remaining three-fourths of the points are obtained by linear interpolation in space. Wind fields must be converted to wind stresses at the surface before they are input to the model. If a more sophisticated time interpolation scheme (than the linear interpolation used in the model) is required, interpolated wind stress fields are included in the data file between the times that actual winds are available.

At an inflow boundary in any layer, the inflow angle and either the velocity magnitude and profile or the transport magnitude and profile can be specified. These quantities are not allow to change with time, except on restart when a new inflow angle and new magnitudes can be specified, and the model will spin up from the old to the new values. At the start of the run the magnitudes spin up from the initial state to the specified values. Outflow boundaries use a radiation condition and do not use any specified data.

3. MODEL PARAMETERS

The model grid for the global ocean model covers the globe from 72°S to 71°N. The horizontal resolution is 0.25° (1/4°), 0.25° latitude by 0.35° longitude.

The atmospheric forcing is introduced through winds into the model. Winds are the only time-dependent forcing, and no synoptic ocean data are assimilated. The model was spun-up from rest to statistical equilibrium using the Hellerman and Rosenstein (1983) monthly mean wind stress climatology. To drive the

model on interannual time scales, 1000-mbar winds from the European Centre for Medium-Range Weather Forecast (ECMWF) were used.

The model was run, for 227 model years for the realistic topography case and for 296 model years for the reduced gravity case, using the wind stress climatology (smoothed monthly mean winds) and, since 1981 it was run with daily averaged ECMWF winds. The ECMWF mean over the 1981-1990 time frame was subtracted from its monthly means and replaced by the Hellerman-Rosenstein annual means. This hybrid wind set was used to extend the integration already spun-up to statistical equilibrium using the Hellerman-Rosenstein monthly winds. Thus, an annual mean solution would still be driven primarily by the Hellerman-Rosenstein data, but seasonal and interannual forcing would come from ECMWF.

ACKNOWLEDGMENTS

Finally, I would like to express my gratitude and appreciation to Dr. Steve Neshyba, Oregon State University, who guided me throughout my initial training in physical oceanography and taught me to love the ocean with all its wonders.

BIBLIOGRAPHY

Brink, K.H., D. Halpern, A. Huyer and R.L. Smith, 1983. The Physical Environment of the Peruvian Upwelling System. *Progress in Oceanography*, **12**, 285-305.

Chen, B., S. R. Smith and D. H. Bromwich, 1996. Evolution of the Tropospheric Split Jet over the South Pacific Ocean during the 1986-89 ENSO Cycle. Monthly Weather Review, **124**, 1,711-1,731.

Fofonoff, N.P. and R.C. Millard, 1983. *Algorithms for Computation of Fundamental Properties of Seawater*. Unesco Technical Papers in Marine Science, **44**, 53 pp.

Fonseca, T., 1989. An overview of the Poleward Undercurrent and Upwelling along the Chilean Coast. In: *Poleward Flows Along Eastern Ocean Boundaries*, S.J. Neshyba,

Heburn, G.W., 1986. The Dynamics of the Western Mediterranean Sea: A Wind Forced Case Study. *Annales Geophysicae*, **5B**, 61-75.

Hellerman, S. and M. Rosenstein , 1983. Normal Monthly Wind Stress over the World Ocean with error estimates. *Journal of Physical Oceanography*, **13**, 1,093-1,104.

Hurlburt, H.E. and J.D. Thompson, 1980. The Dynamics of the Loop Current and Shed Eddies in a Numerical Model of the Gulf of Mexico. *Journal of Physical Oceanography,* **10**, 1,611-1,651.

Hurlburt, H.E. and J.D. Thompson, 1984. Preliminary Results from a Numerical Study of the New England Seamount Chain Influence on the Gulf Stream. *Predictability of Fluid Motions,* G. Holloway and B.J. West, eds., American Institute of Physics, New York, 489-504.

Huyer, A., M. Knoll, T. Paluszkiewicz and R.L. Smith, 1991. The Peru Undercurrent: A study in Variability. *Deep Sea Research,* **38**, Suppl. 1, S247-S271.

Keffer, T., 1985. The Ventilation of the World's Oceans: Maps of Potential Vorticity Field. *Journal of Physical Oceanography,* **15**, 509-523.

McDowell, S., P. Rhines and T. Keffer, 1982. North Atlantic Potential Vorticity and Its Relation to the General Circulation. *Journal of Physical Oceanography,* **12**, 1417-1436.

Neshyba, S. and R. Méndez, 1976. Análisis de Temperaturas Superficiales del Mar como Indicadores de Movimientos de Aguas Superficiales en el Pacífico Sur-Este. *Revista Comisión Permanente del Pacífico Sur,* **5**, 129-137.

Neshyba, S. And T. R. Fonseca, 1980. Evidence for Counterflow to the West Wind Drift off South America. *Journal of Geophysical Research,* **85**, 4888-4892.

Neumann, G., 1968. *Ocean Currents.* Elsevier Publishing Company, 352 pp.

Orlanski, I., 1976. A Simple Boundary Condition for Unbounded Hyperbolic Flows. *Journal of Computational Physics.* **21**, 251-269.

Parfit, M., 1995. Diminishing Returns: Exploiting the Ocean's Bounty. *National Geographic*, **188** (5), 2-37.

Pedlosky, J., 1996. *Ocean Circulation Theory*. Springer-Verlag, 453 pp.

Pond, S. and G.L. Pickard, 1986. Introductory Dynamical Oceanography. 2d ed. Pergamon Press, 329 pp.

Reid, J.L., 1965. Intermediate Waters of the Pacific Ocean. *The John Hopkins Oceanographic Studies*. The John Hopkins Press, 85 pp.

Roache, P.J., 1976. *Computational Fluid Dynamics*. Hermosa Publishers, New Mexico, 446 pp.

Schwerdtfeger, W., 1976. *Climates of Central and South America*. Elsevier Scientific Publishing Company, New York, 532 pp.

Silva, N. and S. Neshyba, 1979. On the Southernmost Extension of the Peru-Chile Undercurrent. *Deep Sea Research*, **26**, Suppl. 1, 1387-1393.

Silva, S., H. Sievers and R. Prado, 1995. Características Oceanográficas y una Proposición de Circulación para algunos Canales Australes de Chile, entre 41° 20' S - 46° 40' S. *Revista de Biología Marina*. **30** (2), 207-254.

SHOA, 1997. *World Ocean Circulation Experiment PR-14, Data Report*. Servicio Hidrográfico y Oceanográfico de la Armada de Chile. To be submitted in 1997 to WOCE Hydrographic Program Office (SCRIPPS, USA).

Strub, T.P., J. Mesías, V. Montecino, J. Rutllant and S. Salinas, 1996. Coastal Ocean Circulation Off Western South America. Accepted for publication in *The Sea,* **10**, 34 pp.

US WOCE, 1986. *U.S. WOCE Planning Report Number 3: Contributions to the planning of WOCE.* US Planning Office for WOCE, Department of Oceanography, Texas A&M University, 229 pp.

Wallcraft, A.J., 1991. The Navy Layered Ocean Model User's Guide. *NOARL report 35.* 21 pp. Naval Oceanographic and Atmospheric Research Laboratory, Stennis Space Center, Mississippi.

Warren, B.A., 1973. Transpacific Hydrographic Sections at Lats. 43°S and 28°S: The SCORPIO Expedition - II. Deep Water. *Deep Sea Research,* **29**, 9-38.

WCRP, 1986. *Scientific Plan for the World Ocean Circulation Experiment.* World Climate Research Programme, WCRP Report No. **6**, 83 pp. WMO/TD - No. 122.

Wyrtki, K., 1963. The Horizontal and Vertical Field of Motion in the Peru Current. *Bulletin of the Scripps Institution of Oceanography of the University of California,* **8**, 313-346.

FIGURES
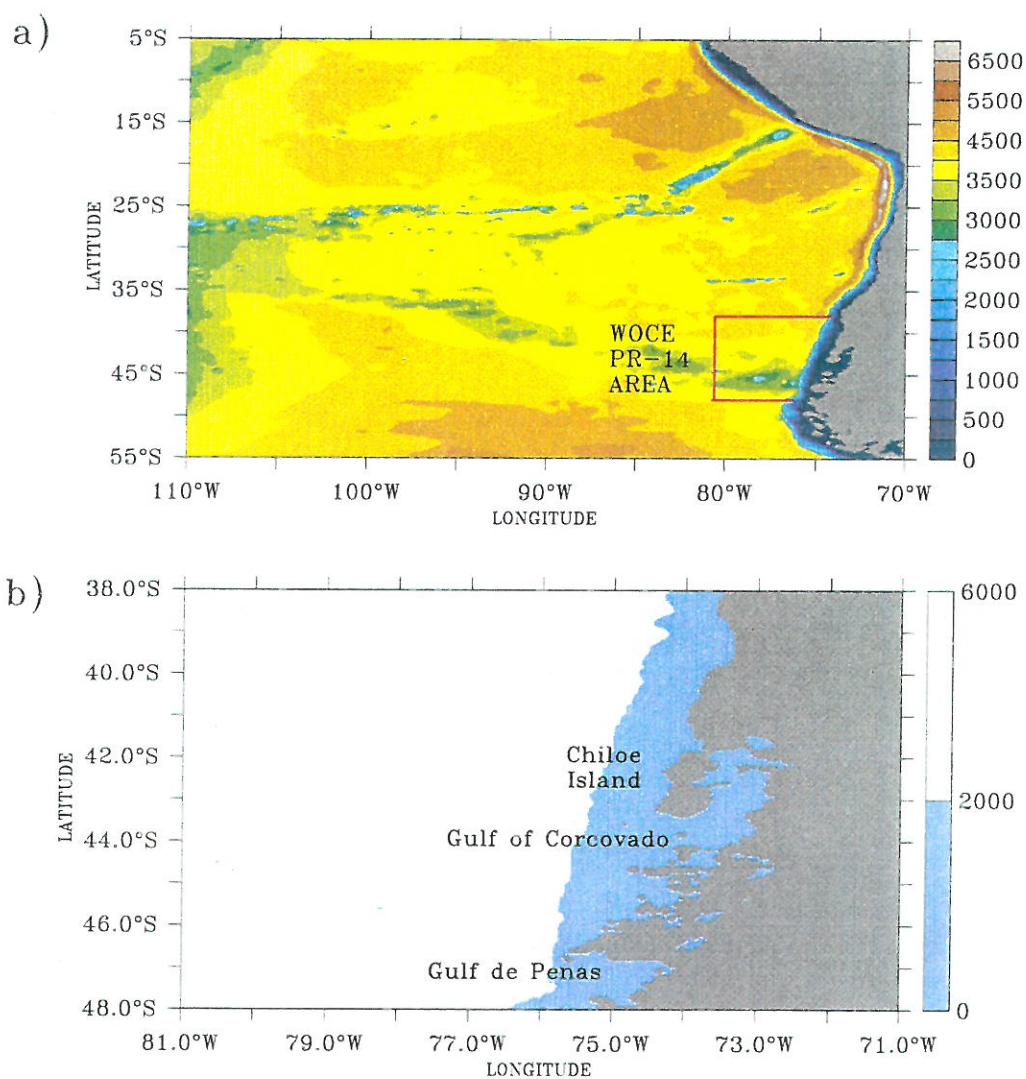
Figure 1: a) NRL Global Ocean Model Sub-Domain (5°S - 55°S, 70°W - 110°W) and WOCE PR-14 sampling area (indicated by red rectangle). b) WOCE PR-14 sampling area. Light blue shaded region indicates water depths less than 2000 meters. Color bar on right-hand side indicates water depth in meters.
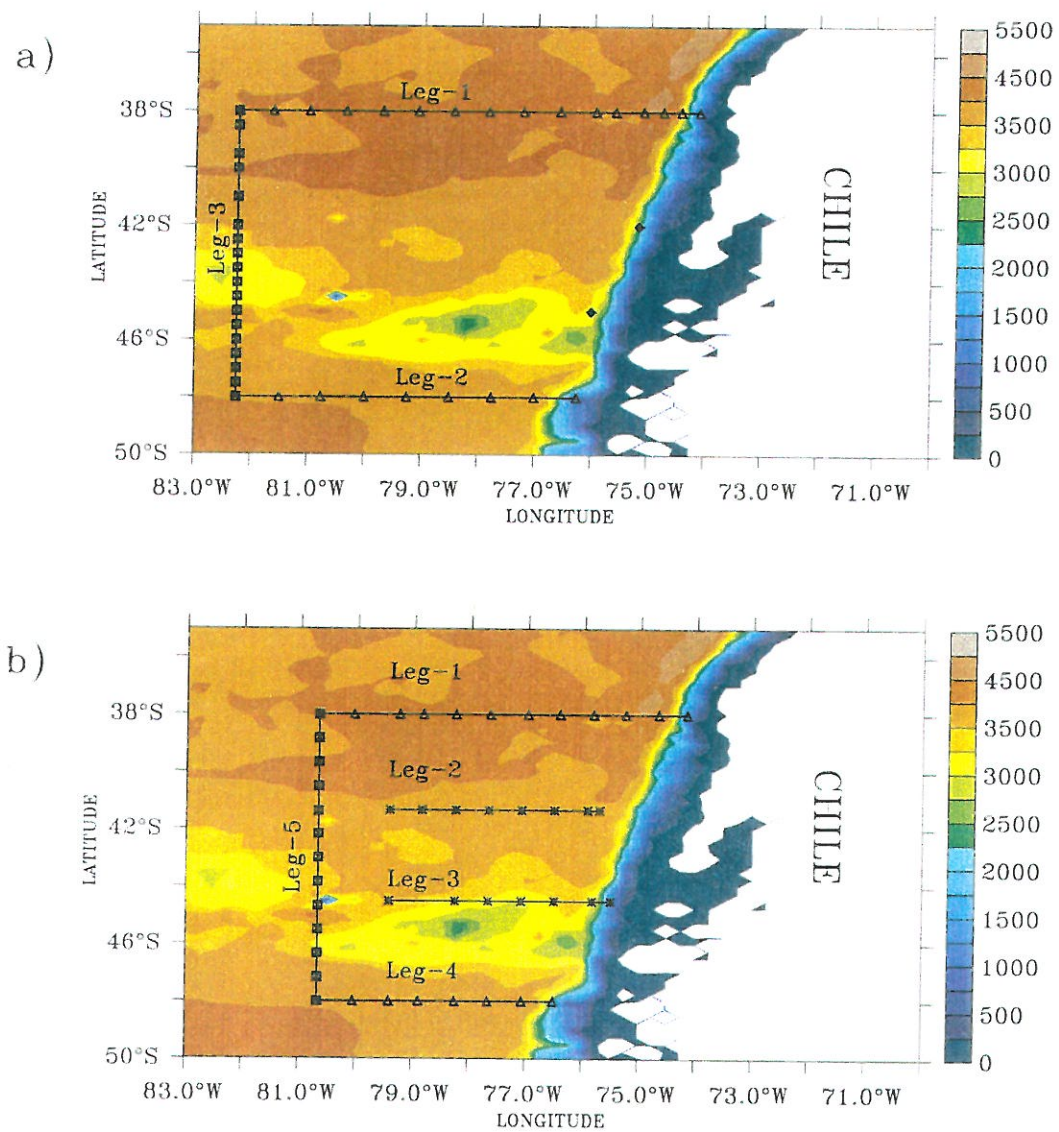
Figure 2: a) WOCE PR-14 cruise track for 1993. b) WOCE PR-14 cruise tracks for 1994 and 1995. Color bar on right-hand side indicates water depth in meters. Symbols drawn on legs indicate the geographic location of each hydrographic station.
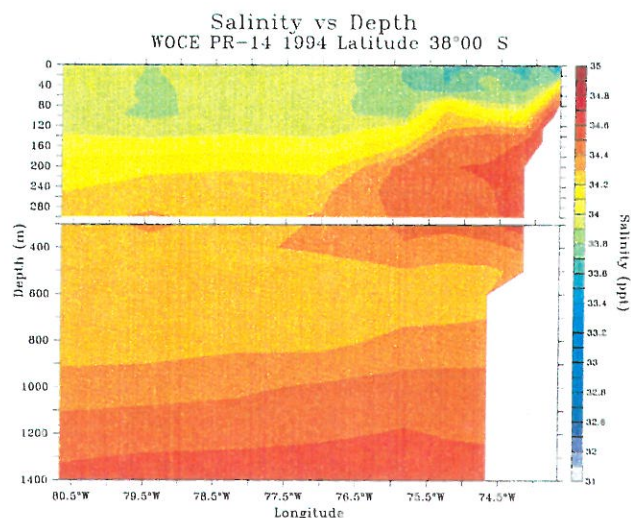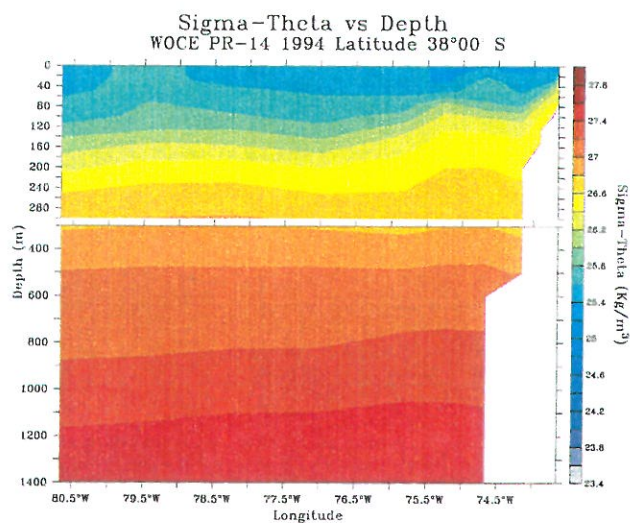
Figure 3: Cross-shelf section of salinity at latitude 38° 00' South during WOCE cruise PR-14 in 1994. The upper part of the figure represents the first 300 meters of the water column. The bottom part goes from 300 to 1400 meters. Color bar on right-hand side indicates the salinity in parts per thousand.
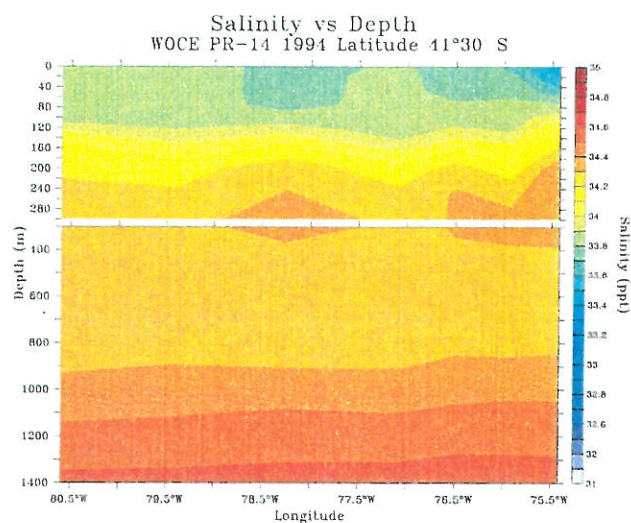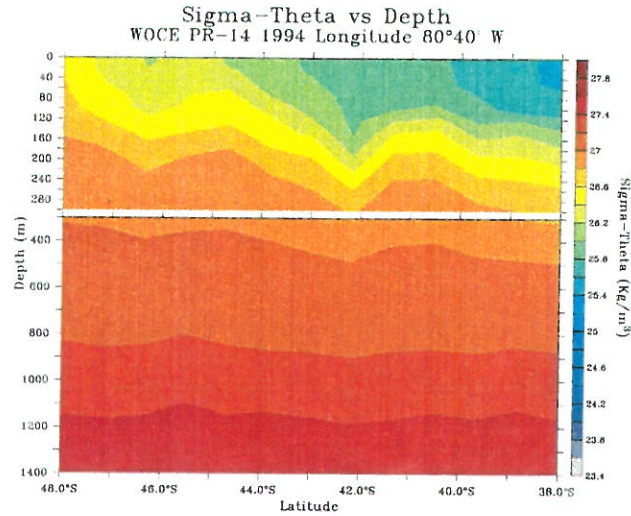

Figure 4: Cross-shelf section of salinity at latitude 41° 30' South during WOCE cruise PR-14 in 1994. The upper part of the figure represents the first 300 meters of the water column. The bottom part goes from 300 to 1400 meters. Color bar on right-hand side indicates the salinity in parts per thousand.
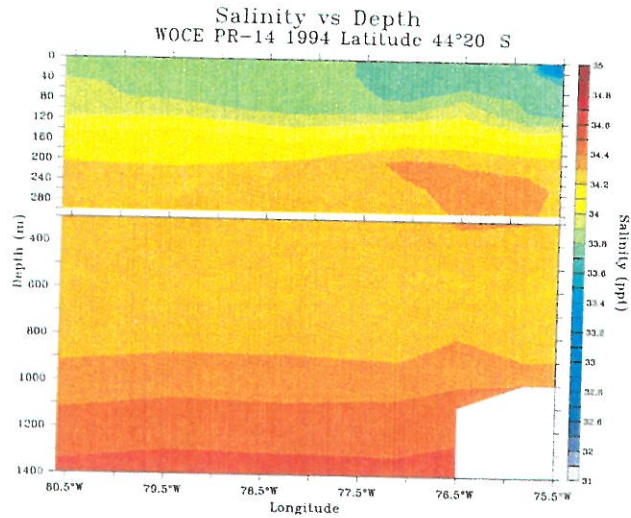
Figure 5: Cross-shelf section of salinity at latitude 44° 20' South during WOCE cruise PR-14 in 1994. The upper part of the figure represents the first 300 meters of the water column. The bottom part goes from 300 to 1400 meters. Color bar on right-hand side indicates the salinity in parts per thousand.
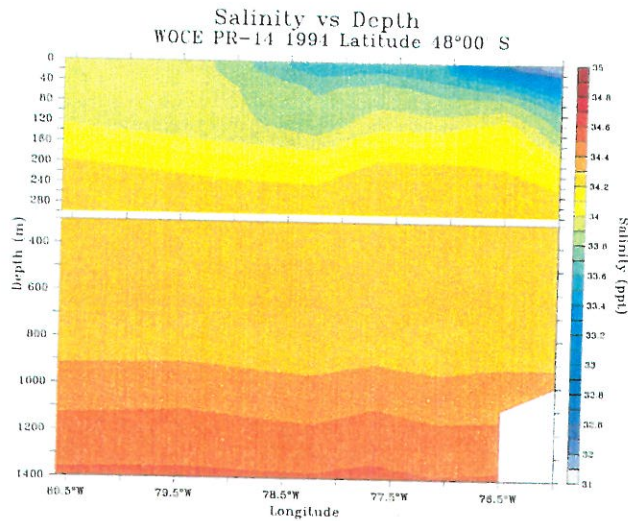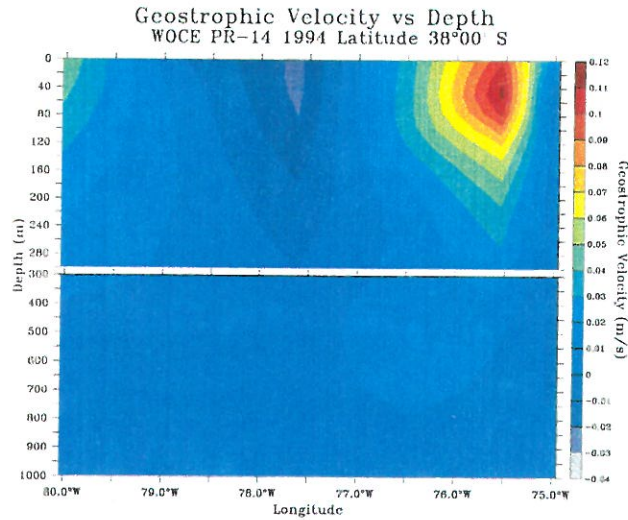

Figure 6: Cross-shelf section of salinity at latitude 48° 00' South during WOCE cruise PR-14 in 1994. The upper part of the figure represents the first 300 meters of the water column. The bottom part goes from 300 to 1400 meters. Color bar on right-hand side indicates the salinity in parts per thousand.
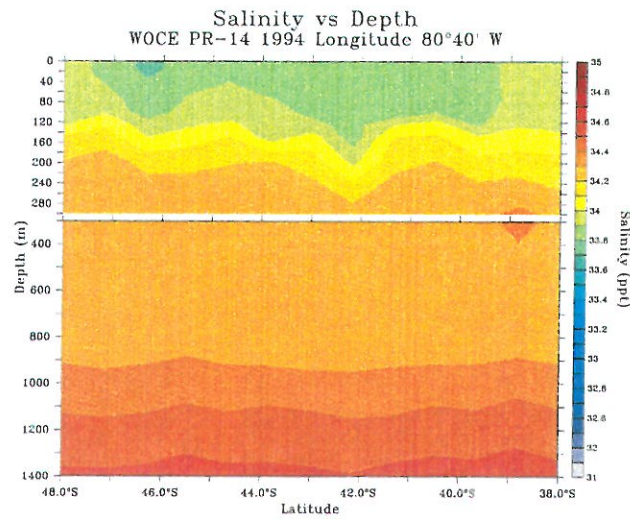
Figure 7: Vertical distribution of salinity along longitude 080° 40' West during WOCE cruise PR-14 in 1994. The upper part of the figure represents the first 300 meters of the water column. The bottom part goes from 300 to 1400 meters. Color bar on right-hand side indicates the salinity in parts per thousand.
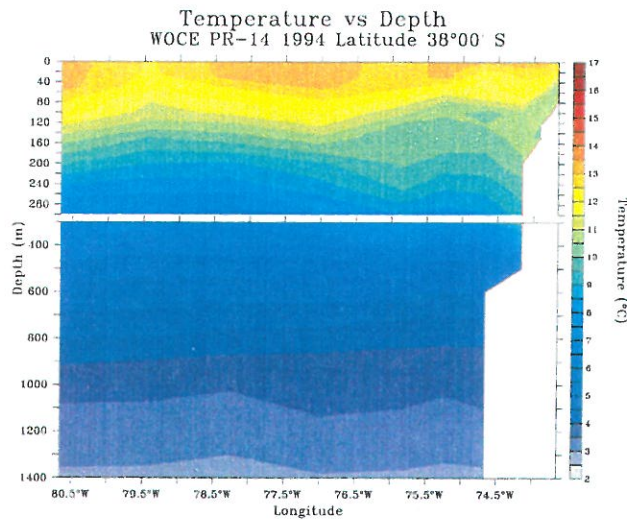
Figure 8: Cross-shelf section of temperature at latitude 38° 00' South during WOCE cruise PR-14 in 1994. The upper part of the figure represents the first 300 meters of the water column. The bottom part goes from 300 to 1400 meters. Color bar on right-hand side indicates the temperature in degrees Celcius.

Temperature vs Depth
WOCE PR–14 1995 Latitude 38°00' S
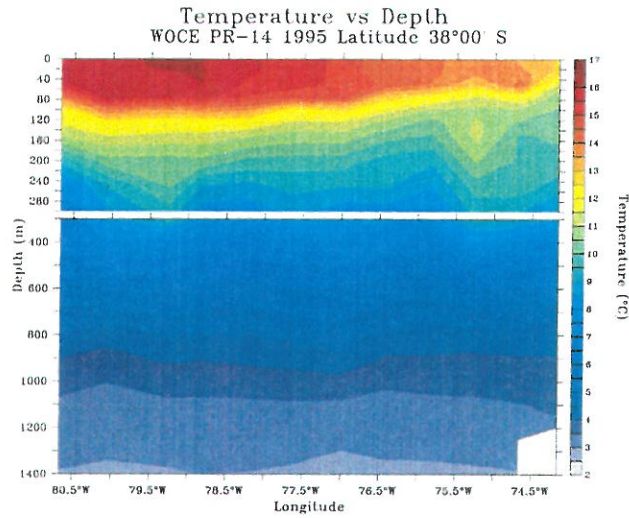
Figure 9: Cross-shelf section of temperature at latitude 38° 00' South during WOCE cruise PR-14 in 1995. The upper part of the figure represents the first 300 meters of the water column. The bottom part goes from 300 to 1400 meters. Color bar on right-hand side indicates the temperature in degrees Celcius.

Temperature vs Depth
WOCE PR–14 1994 Longitude 80°40' W
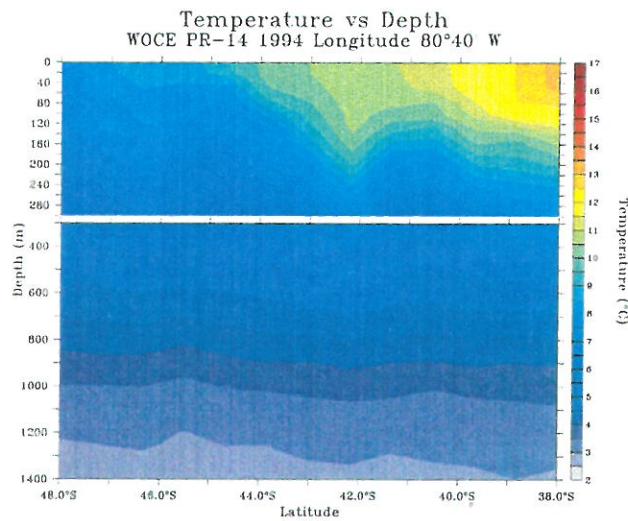
Figure 10: Vertical distribution of temperature along longitude 080° 40' West during WOCE cruise PR-14 in 1994. The upper part of the figure represents the first 300 meters of the water column. The bottom part goes from 300 to 1400 meters. Color bar on right-hand side indicates the temperature in degrees Celcius.
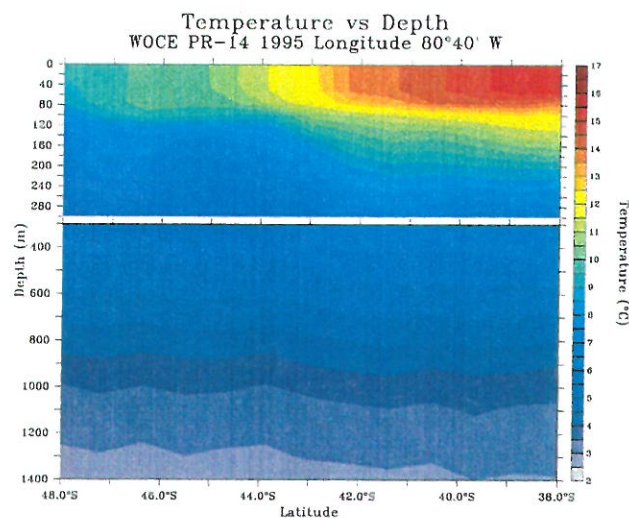
Figure 11: Vertical distribution of temperature along longitude 080° 40' West during WOCE cruise PR-14 in 1994. The upper part of the figure represents the first 300 meters of the water column. The bottom part goes from 300 to 1400 meters. Color bar on right-hand side indicates the temperature in degrees Celcius.

Figure 12: Cross-shelf section of density at latitude 38° 00' South during WOCE cruise PR-14 in 1994. The upper part of the figure represents the first 300 meters of the water column. The bottom part goes from 300 to 1400 meters. Color bar on right-hand side indicates the density in kg/m'3.

Sigma-Theta vs Depth
WOCE PR-14 1994 Longitude 80°40' W

Figure 13: Vertical distribution of density along longitude 080° 40' West during WOCE cruise PR-14 in 1994. The upper part of the figure represents the first 300 meters of the water column. The bottom part goes from 300 to 1400 meters. Color bar on right-hand side indicates the density in kg/m/3.

Geostrophic Velocity vs Depth
WOCE PR-14 1994 Latitude 38°00' S

Figure 14: Cross-shelf section of geostrophic velocity at latitude 38° 00' South during WOCE cruise PR-14 in 1994. Reference level (level of no motion) is 1000 meters. The upper part of the figure represents the first 300 meters of the water column. The bottom part goes from 300 to 1000 meters. Color bar on right-hand side indicates the geostrophic velocity in m/s. Positive values indicate northward velocities.
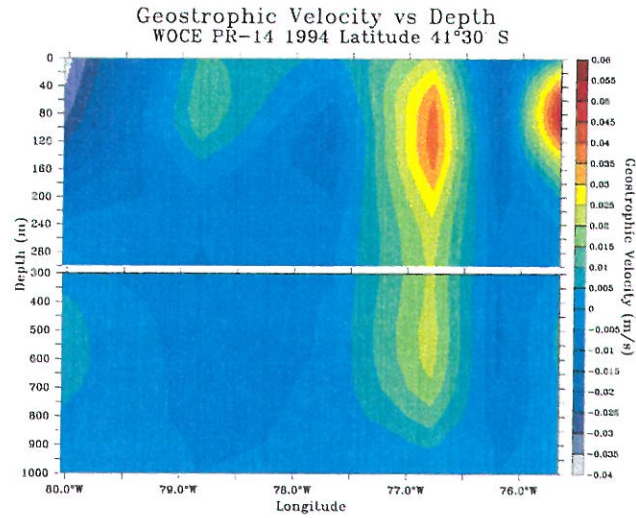
Figure 15: Cross-shelf section of geostrophic velocity at latitude 41° 30' South during WOCE cruise PR-14 in 1994. Reference level (level of no motion) is 1000 meters. The upper part of the figure represents the first 300 meters of the water column. The bottom part goes from 300 to 1000 meters. Color bar on right-hand side indicates the geostrophic velocity in m/s. Positive values indicate northward velocities.
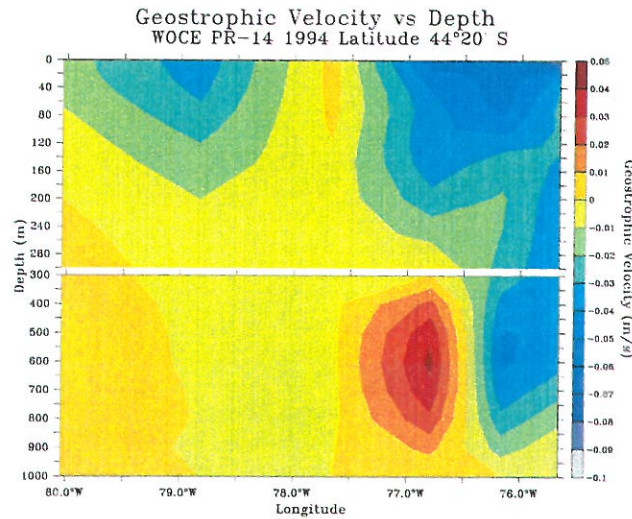
Figure 16: Cross-shelf section of geostrophic velocity at latitude 44° 20' South during WOCE cruise PR-14 in 1994. Reference level (level of no motion) is 1000 meters. The upper part of the figure represents the first 300 meters of the water column. The bottom part goes from 300 to 1000 meters. Color bar on right-hand side indicates the geostrophic velocity in m/s. Positive values indicate northward velocities.

Geostrophic Velocity vs Depth
WOCE PR-14 1994 Latitude 48°00 S
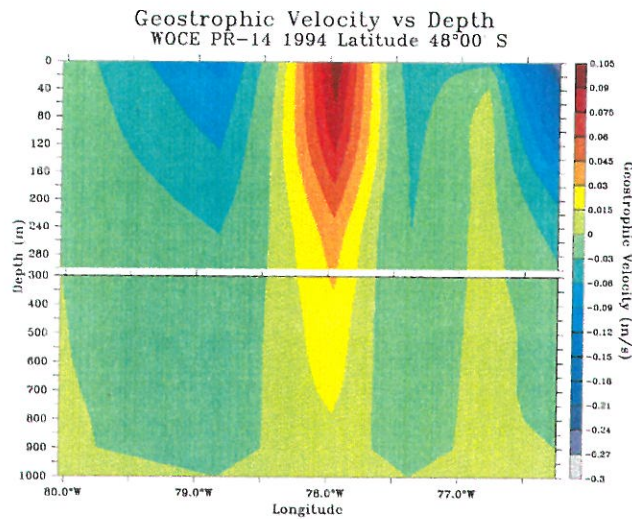
Figure 17: Cross-shelf section of geostrophic velocity at latitude 48° 00' South during WOCE cruise PR-14 in 1994. Reference level (level of no motion) is 1000 meters. The upper part of the figure represents the first 300 meters of the water column. The bottom part goes from 300 to 1000 meters. Color bar on right-hand side indicates the geostrophic velocity in m/s. Positive values indicate northward velocities.

Geostrophic Velocity vs Depth
WOCE PR-14 1994 Longitude 80°40' W
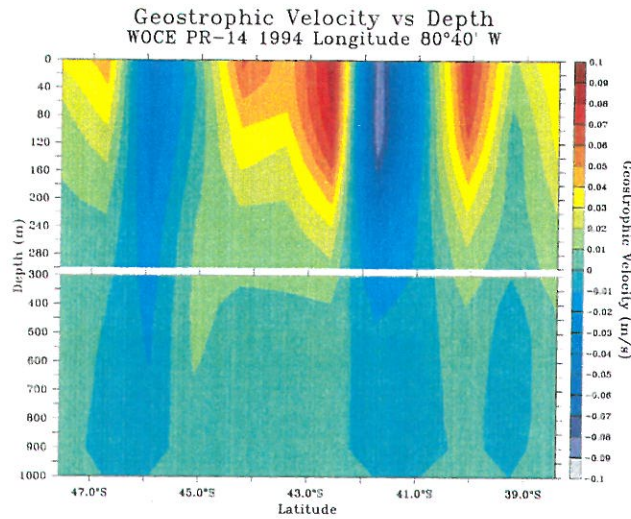
Figure 18: Vertical distribution of geostrophic velocity along longitude 080° 40' West during WOCE cruise PR-14 in 1994. Reference level (level of no motion) is 1000 meters. The upper part of the figure represents the first 300 meters of the water column. The bottom part goes from 300 to 1000 meters. Color bar on right-hand side indicates the geostrophic velocity in m/s. Positive values indicate eastward velocities.

ECMWF Averaged Surface Wind Stress
(October 6 to October 22, 1994)
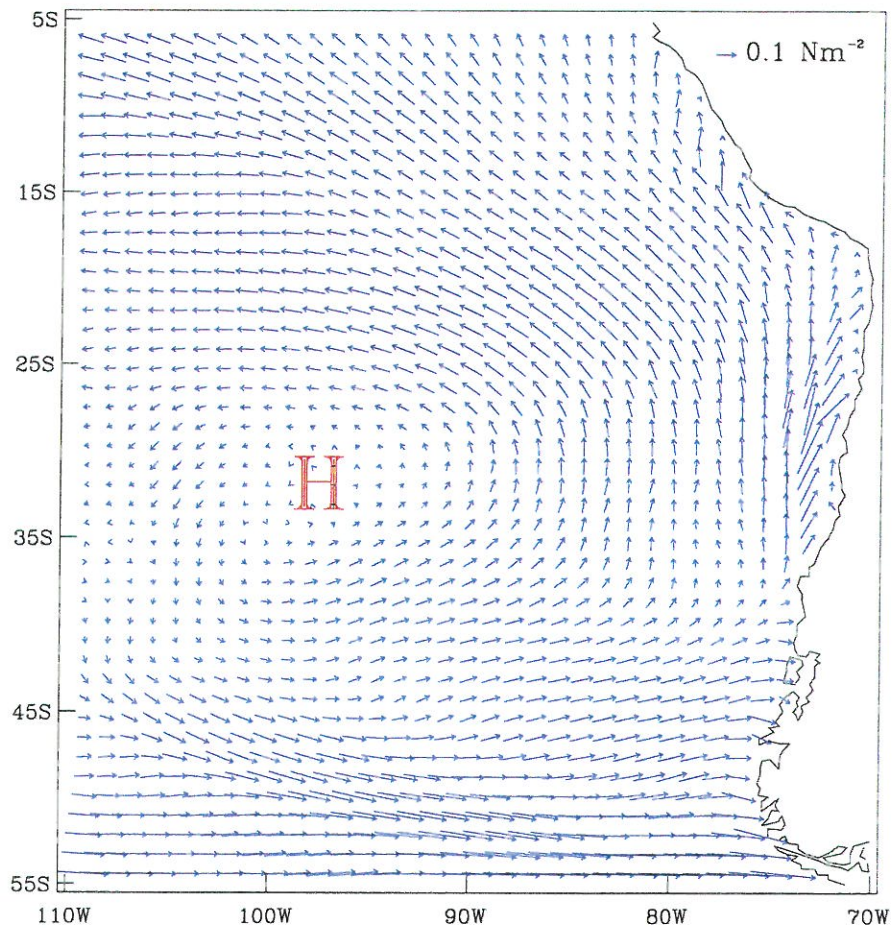
Figure 19: ECMWF averaged surface wind stress for the same period of the WOCE cruise PR-14 in 1994 (October 6 to October 22, 1994). The "H" indicates the location of the South Pacific High. A reference scale in N/m^2 is shown in the upper right corner.

Interpolated Potential Vorticity Field (26.2-27.2)
WOCE PR-14 Oct/06-22 1994
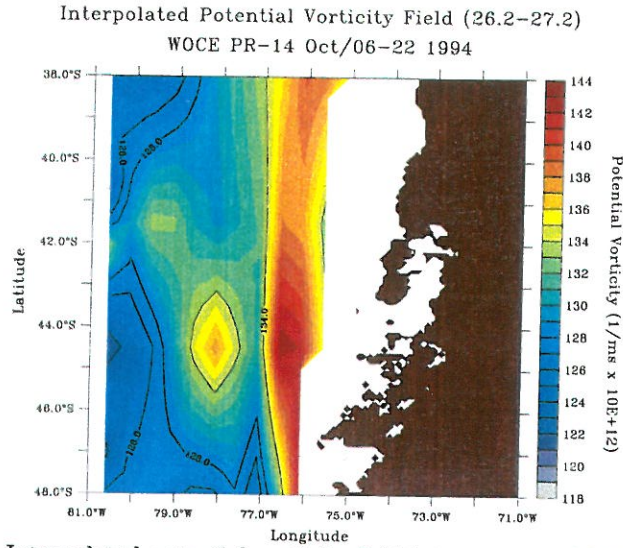
Figure 20: Interpolated potential vorticity field between $\sigma_\theta = 26.2$ kg/m^3 and $\sigma_\theta = 27.2$ kg/m^3 during WOCE cruise PR-14 in 1994. Contour lines are used to underline the proposed flow paths. Color bar on right-hand side indicates potential vorticity in 1/ms x 10E12.

Interpolated Potential Vorticity Field (26.2-26.7)
WOCE PR-14 Oct/06-22 1994
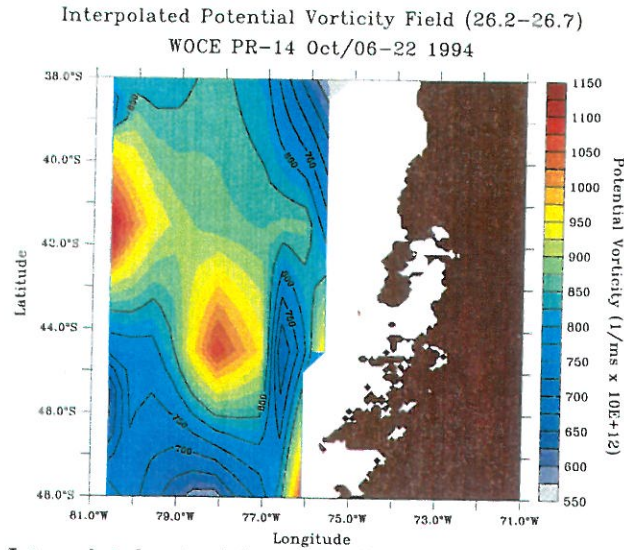
Figure 21: Interpolated potential vorticity field between $\sigma_\theta = 26.2$ kg/m^3 and $\sigma_\theta = 26.7$ kg/m^3 during WOCE cruise PR-14 in 1994. Contour lines are used to underline the proposed flow paths. Color bar on right-hand side indicates potential vorticity in 1/ms x 10E12.

85
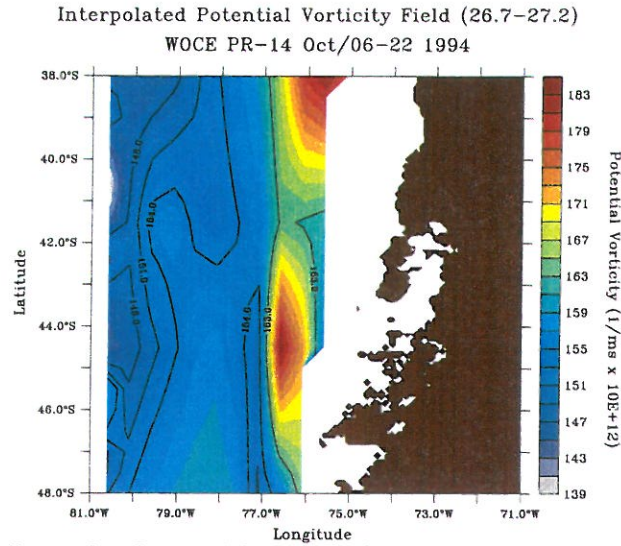
Figure 22: Interpolated potential vorticity field between $\sigma_\theta = 26.7$ kg/m^3 and $\sigma_\theta = 27.2$ kg/m^3 during WOCE cruise PR-14 in 1994. Contour lines are used to underline the proposed flow paths. Color bar on right-hand side indicates potential vorticity in 1/ms x 10E12.
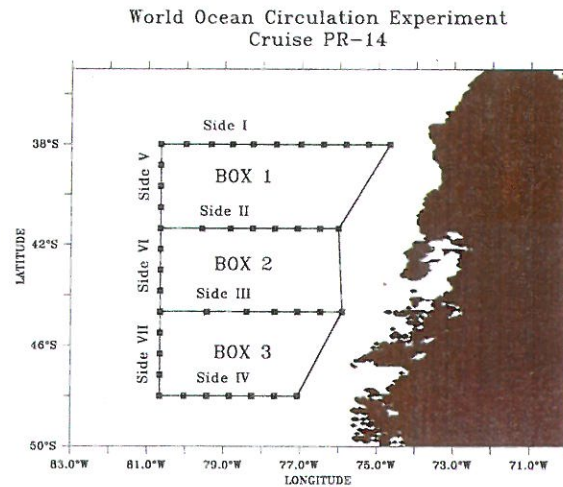
Figure 23: Schematic diagram of the boxes used to calculate the net transport derived from the geostrophic velocity fields. The geographic coordinates of each side of the boxes correspond to the latitudes and longitudes defined for legs 1 through 5 in figure 2b and section 2.1 "Hydrographic Data".

86
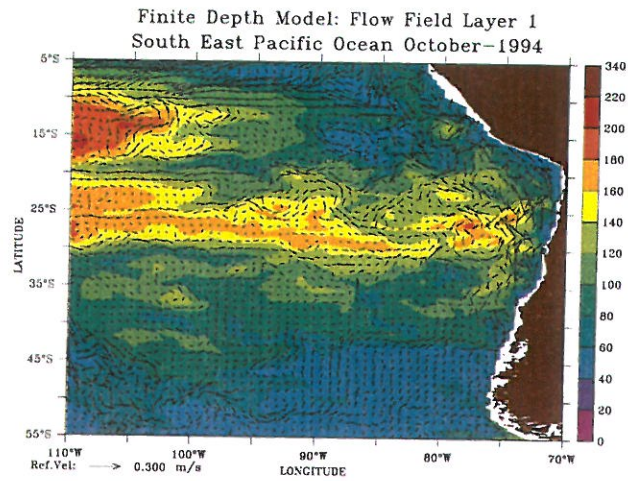
Figure 24: Finite Depth Model - South East Pacific Ocean Region: Average of layer 1 flow fields (vectors) and interface depths (color contours) for October 1994. A reference velocity scale in m/s is shown in the lower left corner. Color bar on right-hand side indicates the depth in meters of the interface between layer 1 and layer 2.
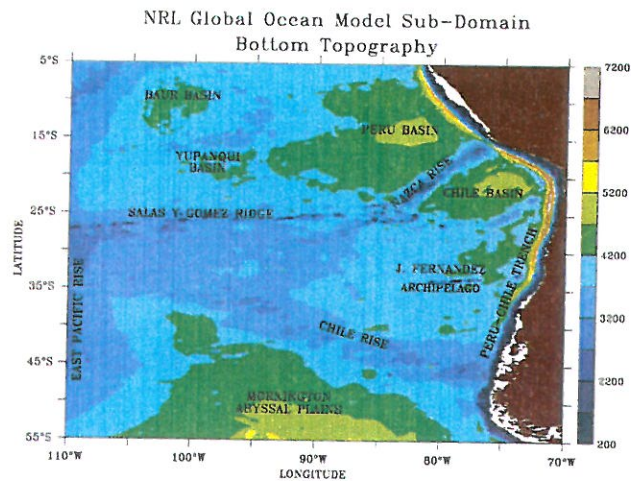

Figure 25: Bottom topography of NRL Global Ocean Model Sub-Domain. White area between first depth contour and coast corresponds to depths of 200 meters or less. Color bar on right-hand side indicates depth in meters. Major topographic features are labeled on plot.

87

Reduced Gravity Model: Flow Field Layer 1
South East Pacific Ocean October–1994
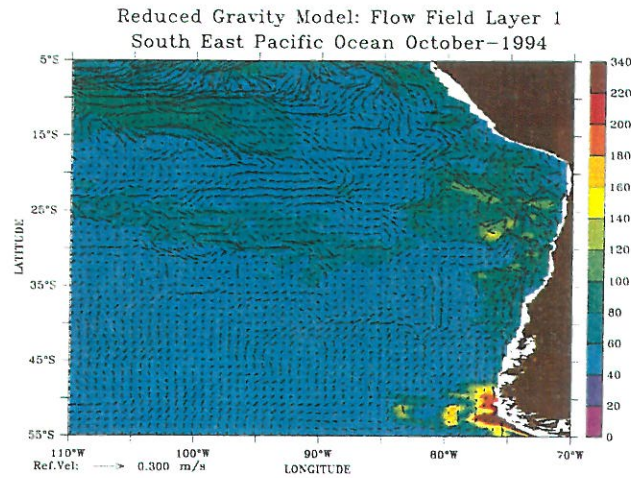
Figure 26: Reduced Gravity Model - South East Pacific Ocean Region: Average of layer 1 flow fields (vectors) and interface depths (color contours) for October 1994. A reference velocity scale in m/s is shown in the lower left corner. Color bar on right-hand side indicates the depth in meters of the interface between layer 1 and layer 2.
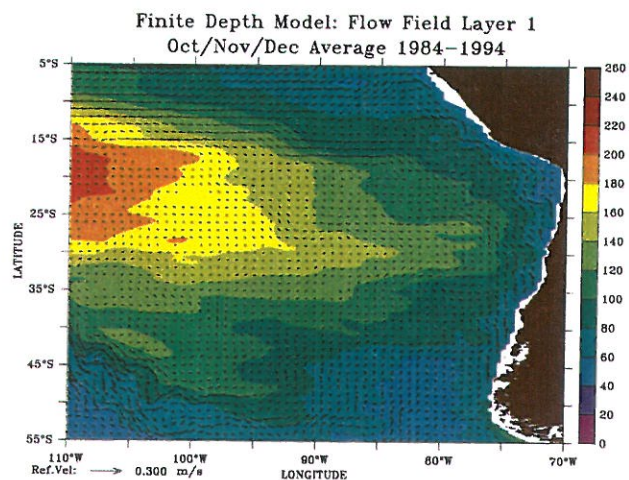

Finite Depth Model: Flow Field Layer 1
Jan/Feb/Mar Average 1984–1994
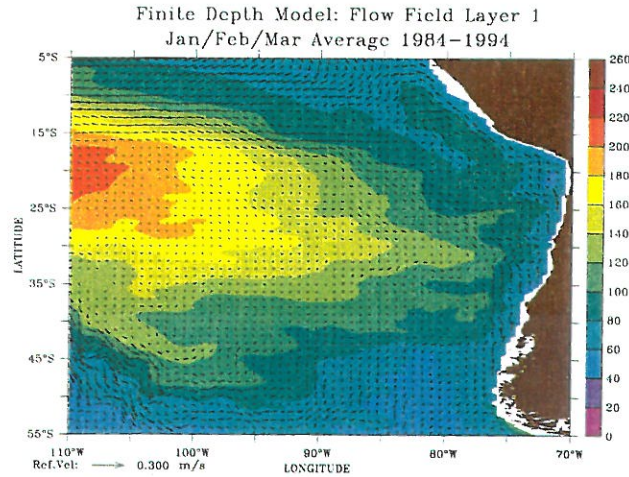
Figure 27: Finite Depth Model - South East Pacific Ocean Region: January-February-March average of layer 1 flow fields (vectors) and interface depths (color contours) between 1984 and 1994. A reference velocity scale in m/s is shown in the lower left corner. Color bar on right-hand side indicates the depth in meters of the interface between layer 1 and layer 2.
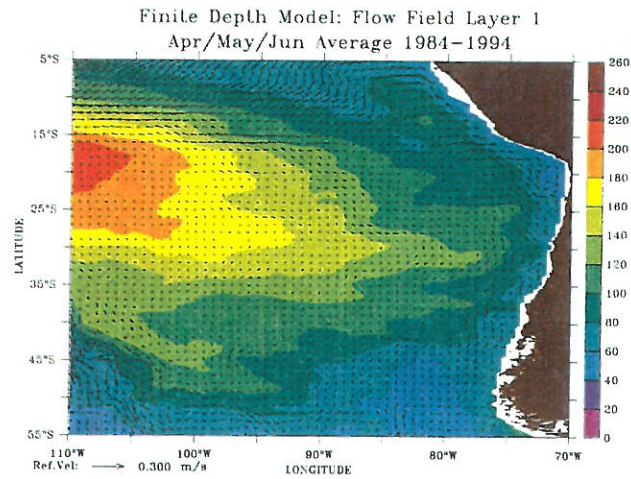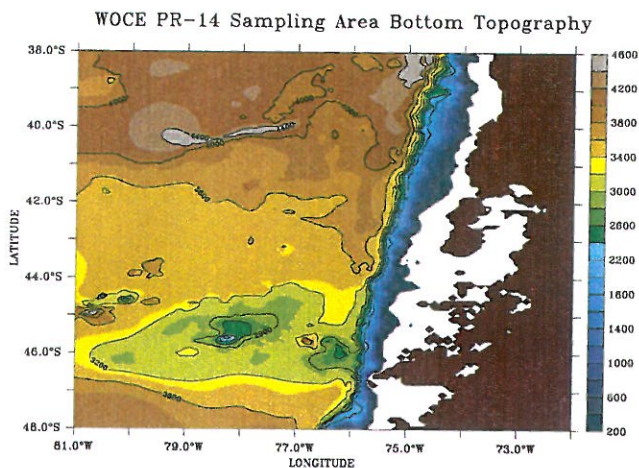
Figure 28: Finite Depth Model - South East Pacific Ocean Region: April-May-June average of layer 1 flow fields (vectors) and interface depths (color contours) between 1984 and 1994. A reference velocity scale in m/s is shown in the lower left corner. Color bar on right-hand side indicates the depth in meters of the interface between layer 1 and layer 2.
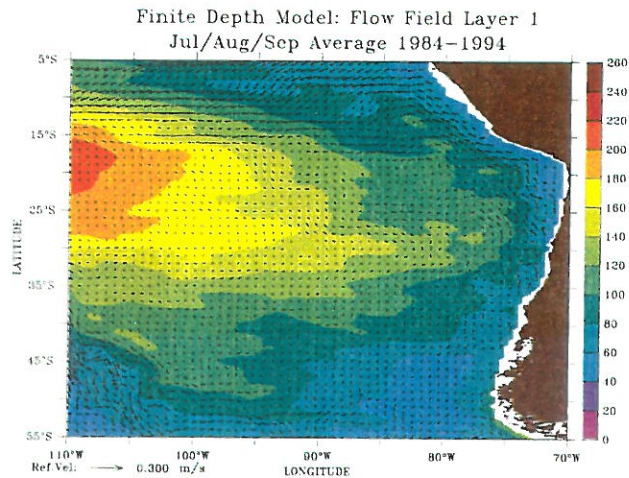
Figure 29: Finite Depth Model - South East Pacific Ocean Region: July-August-September average of layer 1 flow fields (vectors) and interface depths (color contours) between 1984 and 1994. A reference velocity scale in m/s is shown in the lower left corner. Color bar on right-hand side indicates the depth in meters of the interface between layer 1 and layer 2.

Figure 30: Finite Depth Model - South East Pacific Ocean Region: October-November-December average of layer 1 flow fields (vectors) and interface depths (color contours) between 1984 and 1994. A reference velocity scale in m/s is shown in the lower left corner. Color bar on right-hand side indicates the depth in meters of the interface between layer 1 and layer 2.


Figure 31: WOCE PR-14 Sampling Area bottom topography. White area between first depth contour and coast corresponds to depths of 200 meters or less. Some of the depth contours are labeled to help identify the extension of the Chile Rise (Figure 25). Color bar on right-hand side indicates depth in meters.
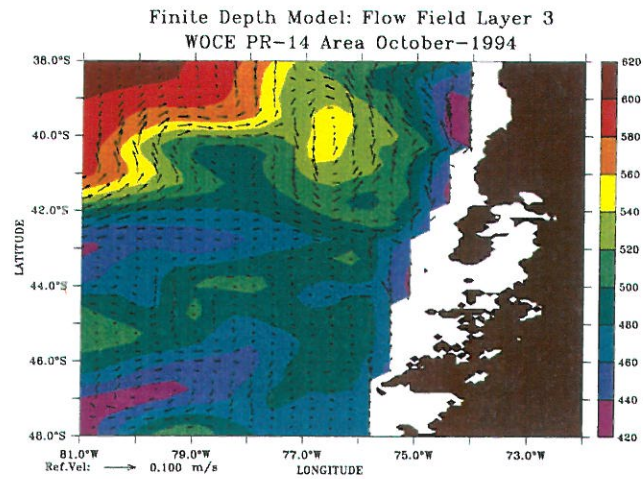
90
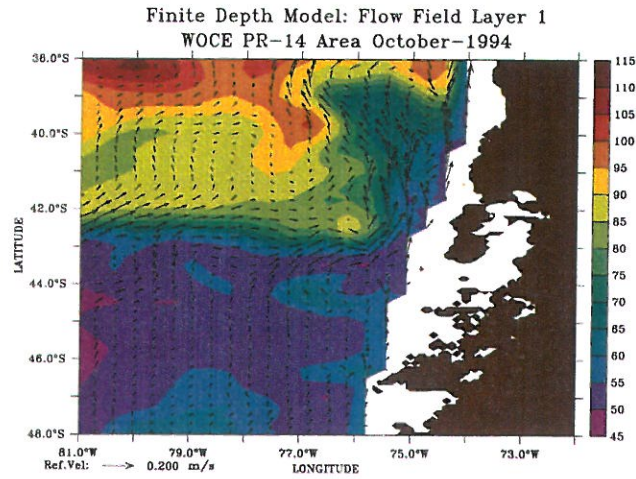
Figure 32: Finite Depth Model - WOCE PR-14 Sampling Area: Average of layer 1 flow fields (vectors) and interface depths (color contours) for October 1994. A reference velocity scale in m/s is shown in the lower left corner. Color bar on right-hand side indicates the depth in meters of the interface between layer 1 and layer 2.
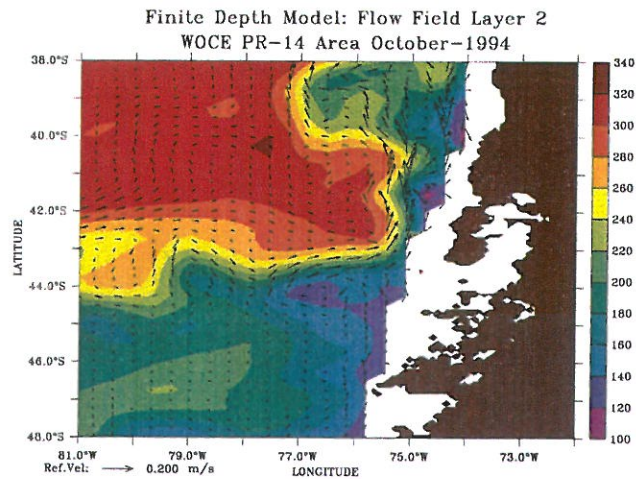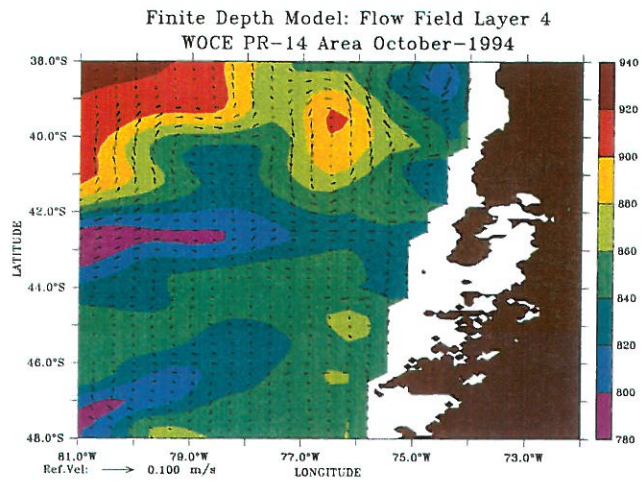

Figure 33: Finite Depth Model - WOCE PR-14 Sampling Area: Average of layer 2 flow fields (vectors) and interface depths (color contours) for October 1994. A reference velocity scale in m/s is shown in the lower left corner. Color bar on right-hand side indicates the depth in meters of the interface between layer 2 and layer 3.

Finite Depth Model: Flow Field Layer 3
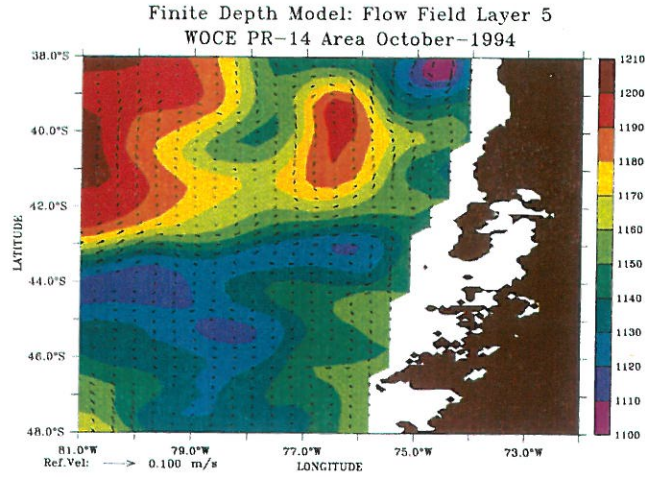WOCE PR−14 Area October−1994

Figure 34: Finite Depth Model - WOCE PR-14 Sampling Area: Average of layer 3 flow fields (vectors) and interface depths (color contours) for October 1994. A reference velocity scale in m/s is shown in the lower left corner. Color bar on right-hand side indicates the depth in meters of the interface between layer 3 and layer 4.

Finite Depth Model: Flow Field Layer 4
WOCE PR−14 Area October−1994

Figure 35: Finite Depth Model - WOCE PR-14 Sampling Area: Average of layer 4 flow fields (vectors) and interface depths (color contours) for October 1994. A reference velocity scale in m/s is shown in the lower left corner. Color bar on right-hand side indicates the depth in meters of the interface between layer 4 and layer 5.
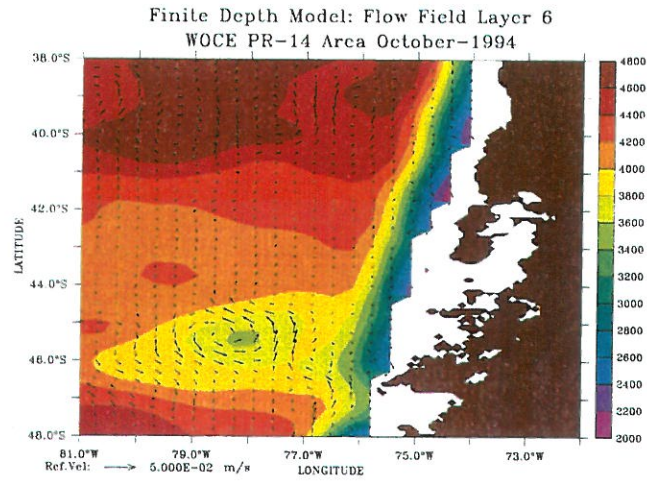
Figure 36: Finite Depth Model - WOCE PR-14 Sampling Area: Average of layer 5 flow fields (vectors) and interface depths (color contours) for October 1994. A reference velocity scale in m/s is shown in the lower left corner. Color bar on right-hand side indicates the depth in meters of the interface between layer 5 and layer 6.

Figure 37: Finite Depth Model - WOCE PR-14 Sampling Area: Average of layer 1 flow fields (vectors) and interface depths (color contours) for October 1994. A reference velocity scale in m/s is shown in the lower left corner. Color bar on right-hand side indicates the depth in meters of layer 6.

Finite Depth Model: Flow Field Layer 1
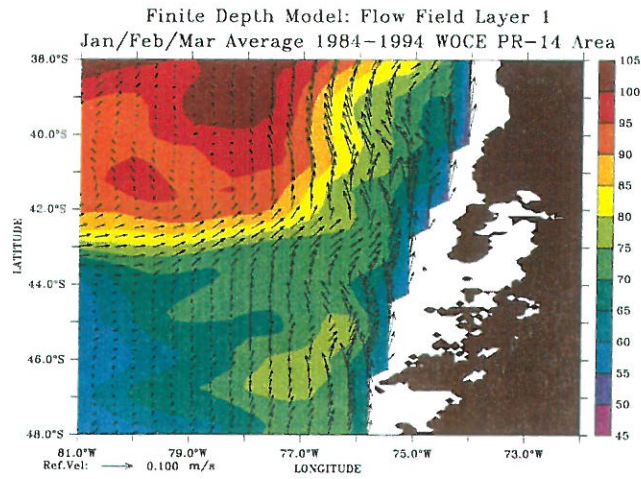**Jan/Feb/Mar Average 1984–1994 WOCE PR–14 Area**

Figure 38: Finite Depth Model - WOCE PR-14 Sampling Area: January-February-March average of layer 1 flow fields (vectors) and interface depths (color contours) between 1984 and 1994. A reference velocity scale in m/s is shown in the lower left corner. Color bar on right-hand side indicates the depth in meters of the interface between layer 1 and layer 2.

Finite Depth Model: Flow Field Layer 1
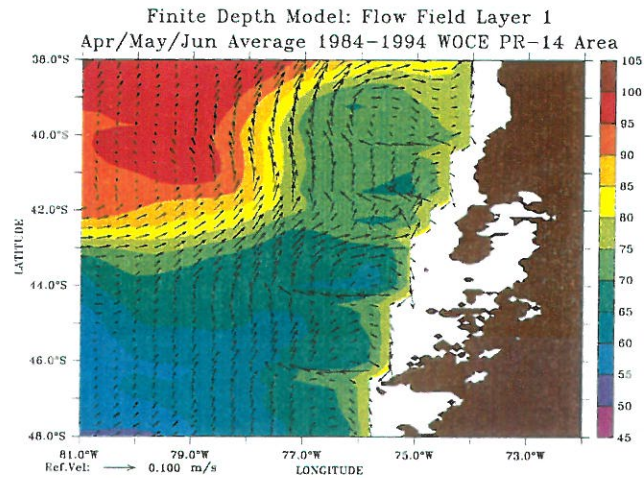**Apr/May/Jun Average 1984–1994 WOCE PR–14 Area**

Figure 39: Finite Depth Model - WOCE PR-14 Sampling Area: April-may-June average of layer 1 flow fields (vectors) and interface depths (color contours) between 1984 and 1994. A reference velocity scale in m/s is shown in the lower left corner. Color bar on right-hand side indicates the depth in meters of the interface between layer 1 and layer 2.
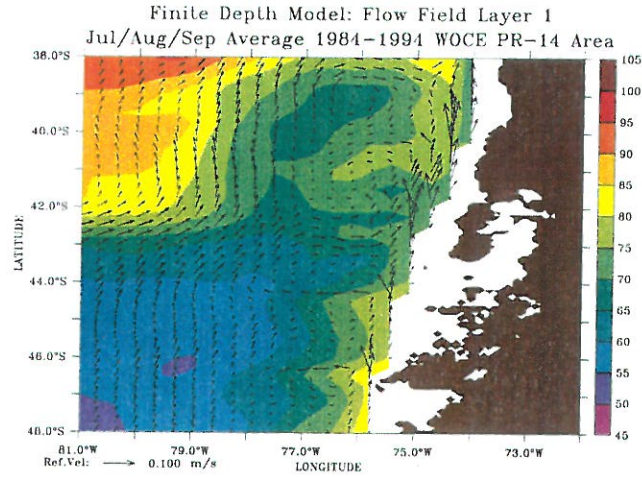
Figure 40: Finite Depth Model - WOCE PR-14 Sampling Area: July-August-September average of layer 1 flow fields (vectors) and interface depths (color contours) between 1984 and 1994. A reference velocity scale in m/s is shown in the lower left corner. Color bar on right-hand side indicates the depth in meters of the interface between layer 1 and layer 2.
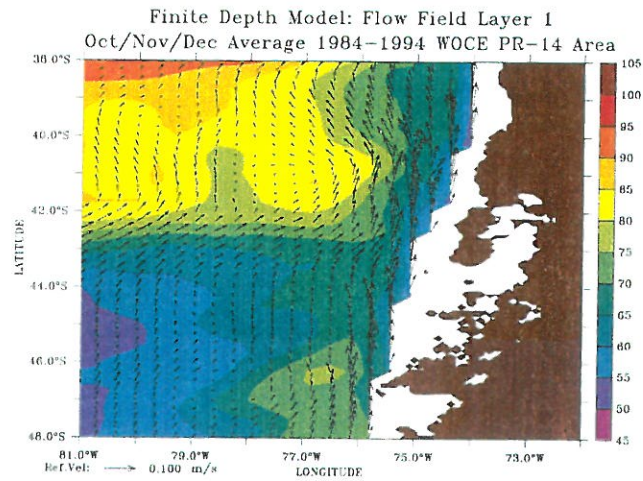

Figure 41: Finite Depth Model - WOCE PR-14 Sampling Area: October-November-December average of layer 1 flow fields (vectors) and interface depths (color contours) between 1984 and 1994. A reference velocity scale in m/s is shown in the lower left corner. Color bar on right-hand side indicates the depth in meters of the interface between layer 1 and layer 2.